



HAL
open science

The Impact of Radial and Non-Radial IMF on the Earth's Magnetopause Size, Shape, and Dawn-Dusk Asymmetry From Global 3D Kinetic Simulations

Suleiman Baraka, Olivier Le Contel, Lotfi Ben-Jaffel, William Moore

► **To cite this version:**

Suleiman Baraka, Olivier Le Contel, Lotfi Ben-Jaffel, William Moore. The Impact of Radial and Non-Radial IMF on the Earth's Magnetopause Size, Shape, and Dawn-Dusk Asymmetry From Global 3D Kinetic Simulations. *Journal of Geophysical Research Space Physics*, 2021, 126 (10), 10.1029/2021JA029528 . hal-03407917

HAL Id: hal-03407917

<https://hal.science/hal-03407917>

Submitted on 9 Nov 2021

HAL is a multi-disciplinary open access archive for the deposit and dissemination of scientific research documents, whether they are published or not. The documents may come from teaching and research institutions in France or abroad, or from public or private research centers.

L'archive ouverte pluridisciplinaire **HAL**, est destinée au dépôt et à la diffusion de documents scientifiques de niveau recherche, publiés ou non, émanant des établissements d'enseignement et de recherche français ou étrangers, des laboratoires publics ou privés.

The impact of Radial and Non-Radial IMF on the Earth's Magnetopause Size, Shape, and Dawn-Dusk Asymmetry from Global 3D Kinetic Simulations

Suleiman M Baraka^{1,3}, O. Le Contel², L. Ben-Jaffel³, W. B. Moore^{1,4}

¹National Institute of Aerospace, 100 Exploration Way, Hampton, VA 23666

²Laboratoire de Physique des Plasmas, UMR7648, CNRS/Sorbonne Université/Université Paris-Saclay/Observatoire de Paris/Ecole Polytechnique Institut Polytechnique de Paris, Palaiseau, France.

³Institut d'Astrophysique de Paris. Sorbonne Universités, UPMC & CNRS, 98 bis Bd. Arago, F-75014 Paris, France

⁴Hampton University, 154 William R. Harvey Way Hampton, VA 23668

Key Points:

- The magnetopause expansion at the subsolar point for radial and non-radial IMF is partly due to the reduction of the solar wind dynamic pressure caused by backstreaming ions.
- Although backstreaming ions constitute only 16.5% and 20% of the solar wind bulk flow for radial and non-radial IMF, they strongly modify the dynamic pressure.
- For both radial and non-radial IMF, the magnetopause is asymmetric, being more extended on the duskside than on the dawnside.

Corresponding author: Suleiman M Baraka, suleiman.baraka@nianet.org

This article has been accepted for publication and undergone full peer review but has not been through the copyediting, typesetting, pagination and proofreading process, which may lead to differences between this version and the [Version of Record](#). Please cite this article as [doi: 10.1029/2021JA029528](https://doi.org/10.1029/2021JA029528).

This article is protected by copyright. All rights reserved.

Abstract

The boundary between the solar wind (SW) and the Earth's magnetosphere, the magnetopause (MP), is highly dynamic. Its location and shape depend on SW dynamic pressure and interplanetary magnetic field (IMF) orientation. We use a 3D kinetic Particle-In-Cell code (IAPIC) to simulate an event observed by THEMIS spacecraft on July 16, 2007. We investigate the impact of radial ($\theta_{Bx}=0^\circ$) and non-radial ($\theta_{Bx}=50^\circ$) IMF on the shape and size of Earth's MP for a dipole tilt of 31° using maximum density gradient and pressure balance methods. Using the Shue model as a reference (MP at $10.3 R_E$), we find that for non-radial IMF the MP expands by 1.4 and $1.7 R_E$ along the Sun-Earth (OX) and tilted magnetic equatorial (Tilt) axes, respectively, and it expands by 0.5 and $1.6 R_E$ for radial IMF along the same respective axes. When the effect of backstreaming ions is removed from the bulk flow, the expansion ranges are 1.0 and $1.3 R_E$ and 0.2 , and $1.2 R_E$, respectively. It is found that the percentage of backstreaming to bulk flow ions are 16.5% and 20% for radial and non-radial IMF. We also show that when the backstreaming ions are not identified, up to 40% of the observed expansion that is due to backstreaming particles can be inadvertently attributed to a change in the SW upstream properties. Finally, we quantified the temperature anisotropy in the magnetosheath, and observe a strong dawn-dusk asymmetry in the MP location, being more extended on the duskside than on the dawnside.

Plain Language Summary

The Earth's magnetopause (MP) is a sensitive region where the pressure of the Earth magnetic field balances the shocked solar wind ram and thermal pressures. Accurate space weather monitoring and forecast require an in-depth knowledge of this region and of the physical processes that affect it. We investigate the effects of the orientation of the interplanetary magnetic field (IMF) on the MP size, location, and shape by using a numerical technique (3D kinetic simulation) that uses macro-ions and macro-electrons to mimic the real charged species and explicitly resolves their motion. We are able to extract the shape and location of the MP in three dimensions to estimate the sensitivity of the MP position to

48 the ambient IMF and solar wind conditions, while our explicit tracking of ion motions allows
49 us to investigate the role of ion species backscattered by the Earth's bow shock and magne-
50 tosheath. We find that when the IMF has a strong component in the Earth-Sun direction
51 (radial or non-radial IMF), these backscattered ions play an important role in reducing the
52 effective pressure of the incoming solar wind and allowing the MP to expand outward.

Accepted Article

1 Introduction

The magnetic fields of planets such as Mercury, Earth, and the giant planets present an obstacle to the supersonic solar wind (SW). As a result, a shock forms and the solar wind is redirected around the obstacle producing a cavity which is called the magnetosphere (e.g., Parks, 1991). The boundary between the shocked SW and the plasma in the magnetosphere is the magnetopause (MP). At the subsolar point, the classical fluid description of the SW stagnation flow derives the location of the magnetopause by the balance between the planetary magnetic field pressure and the dynamic pressure of the SW. Plasma boundary layers form on either side of the magnetopause with the magnetosheath boundary layer (MSBL) on the sunward side and the low-latitude boundary layer (LLBL) on the magnetosphere side. Both layers play an important role in plasma exchange across the magnetopause (e.g., Pi et al., 2018).

The magnetopause structure is significantly influenced by the interplanetary magnetic field (IMF) orientation. While the impact of southward (Yu & Ridley, 2009; Heikkila, 2011; Tan et al., 2011; Suvorova & Dmitriev, 2015; Berchem et al., 2016) and northward IMF (Sorathia et al., 2019; Luo et al., 2013; Bobra et al., 2004; Wang et al., 2018) on the dynamics of Earth's magnetosphere have been extensively studied in the last four decades, only recently has attention been focused on radially-dominant IMF conditions, which will be called radial IMF for the remainder of this paper. For most solar wind plasma conditions at the orbital position of planets, bow shocks are collisionless and supercritical shocks, which by definition, reflect and accelerate a fraction of the plasma impinging on them. These backstreaming particles lead to the formation of the ion foreshock region upstream (e.g., Turner et al., 2018, p. 206).

Following early satellite observations (Greenstadt et al., 1968; Asbridge et al., 1968), the idea of an extended foreshock that diverts the solar wind around the magnetosphere and reduces the solar wind dynamic pressure at the subsolar magnetopause was proposed for radial IMF conditions (Fairfield et al., 1990; Merka et al., 2003; Jelínek et al., 2010;

80 Suvorova et al., 2010). The distance and shape of the equatorial magnetopause is strongly
81 affected by radial IMF, resulting in a global expansion of the magnetopause (Grygorov et al.,
82 2017). Zhang et al. (2019) found that a dawn-dusk asymmetry exists in the magnetosheath,
83 directly related to the IMF orientation. Evidently, the plasma distribution and the IMF are
84 correlated to these asymmetries which are either generated at the bow shock or inside the
85 magnetosheath itself.

86 Most magnetopause observations during radial IMF have noticed a large magnetopause
87 expansion that was connected with a significant distortion of the magnetopause surface.
88 Large magnetopause distortion and anomalous sunward magnetosheath flows were reported
89 in one radial IMF event by (Shue et al., 2009). The finding of magnetopause displacement
90 during radial IMF conditions was also documented in a statistical study based on a large
91 set of magnetopause crossings using THEMIS (Dušík et al., 2010) and GOES (Park et al.,
92 2016) data. A systematic increase of observed magnetopause distances for radial IMF was
93 found, ranging from $0.3R_E$ at 90° cone angle to $\approx 1.7R_E$ at 0° or 180° cone angles compared
94 to empirical models. However, Dušík et al. (2010); Suvorova and Dmitriev (2015) pointed
95 out a large dispersion in their statistical results attributed to the difficulty to propagate
96 radial IMF to the magnetopause. In contrast, using THEMIS data and empirical models of
97 the MP, Grygorov et al. (2017) concluded that the distance of the equatorial magnetopause
98 is strongly affected by radial IMF, expanding globally and independent of the local time,
99 upstream value of other solar wind parameters or the tilt of the Earth magnetic dipole.

100 It is interesting to remark that no self-consistent model exists today in the literature that
101 can explain the observed MP displacement or its asymmetry, particularly with the difficulty
102 MHD approaches have to accurately model reflected SW ions in the foreshock region (Sibeck
103 et al., 2001). In a recent study, (Samsonov et al., 2017) used previous statistical results to
104 suggest that the density and velocity in the foreshock region decrease to $\sim 60\%$ and $\sim 94\%$
105 of the undisturbed SW values when the cone angle falls below 50° causing a drop in the
106 SW dynamic pressure of $\sim 53\%$ that might cause the MP displacement. In a second step,

107 those authors modified the upstream SW parameters in a global MHD model to take these
108 foreshock effects into account, which helped them predict MP distances during non-radial
109 IMF intervals close to those observed by THEMIS. More precisely, using time dependent SW
110 conditions provided by ACE and WIND measurements in their simulations, they applied
111 a $\sim 53\%$ dynamic pressure reduction as soon as the SW cone angle becomes smaller than
112 50° . This limit was chosen in order to smooth the swap between radial (reduced dynamic
113 pressure) and non-radial (unchanged dynamic pressure) regimes (Samsonov et al., 2017). In
114 the present study, we employ constant upstream SW conditions. For the sake of covering
115 the full range of cone angles considered in the simulations of (Samsonov et al., 2017), we
116 have performed simulations for the two limit cases of 0° (referred to as radial IMF) and
117 $\sim 50^\circ$ cone angle (referred to as non-radial IMF). We note that there is no consistent usage
118 in the literature of the terms radial or non-radial IMF.

119 According to Samsonov et al. (2017), the strong total pressure decrease in data seems to
120 be a local, rather than a global, phenomenon. Those authors conceded that their model was
121 not self-consistent in the sense that the modified upstream SW parameter adjustment was
122 global and not specific to the foreshock region for which the statistical results (discussed
123 above) were initially derived. One of the goals of this study is to investigate the role of
124 backscattered ions in producing decreased SW dynamic pressure ahead of the magnetopause
125 by resolving them in a 3D kinetic simulation.

126 In addition to the expansion of the MP, the other focus of this study is the gener-
127 ation of dawn-dusk asymmetry under radial IMF, which has been investigated for many
128 decades (Akasofu et al., 1982; Akasofu, 1991; Haaland et al., 2017, and references therein).
129 Dawn-dusk asymmetries are ubiquitous features of the coupled solar wind-magnetosphere-
130 ionosphere system. During the last decades, the increasing availability of satellite and
131 ground-based measurements has made it possible to study these phenomena in more de-
132 tail (e.g., B. M. Walsh, 2017). Most studies reported so far agree that the dawn-dusk
133 asymmetry is primarily the result of the Parker spiral solar wind impinging with a specific

134 geometric configuration that impacts and preconditions the magnetosphere (e.g., Haaland
135 et al., 2017, and references therein). Under radial conditions, the IMF and the SW flow
136 are symmetric with respect to the Sun-Earth line. Under those conditions, one cannot in-
137 voke the asymmetry due to the Parker spiral shape to explain any dawn-dusk asymmetry.
138 Therefore, other physical processes, like kinetic effects, should be investigated to explain
139 any potential asymmetry. For instance, statistical studies based on THEMIS and Cluster
140 measurements confirm a rather global expansion of the magnetopause under radial IMF
141 without significant dawn-dusk asymmetries was detected (Zhang et al., 2019). The same
142 statistical study showed that magnetic reconnection (MR) is nearly absent during radial
143 IMF, in contrast to the north IMF conditions during which lobe MR and the consequent
144 dawn-dusk asymmetries are strong (Zhang et al., 2019). However, possible influence of ra-
145 dial IMF on the aurora and dayside magnetic reconnection for different dipole tilt angles
146 have also been investigated by (Østgaard et al., 2003; Zhang et al., 2019).

147 Kinetic effects are expected to trigger a large set of distinct dawn-dusk asymmetries up-
148 stream of the magnetosphere due to the formation of the foreshock region that is connected
149 with solar wind particles backscattered at the bow shock and magnetosheath. Although
150 much of the plasma passes through the bow shock, the reflected population generates a
151 number of plasma instabilities, which trigger waves and generate wave-particle interactions
152 as well as other dynamics at the non-parallel shock that should favor dawn-dusk asymme-
153 tries (e.g., B. M. Walsh, 2017, and references therein). The radial IMF condition would
154 thus be the ideal configuration to reveal such kinetic effects and determine their role in
155 producing the dawn-dusk asymmetry so far observed (Zhang et al., 2019). For reference,
156 using Cluster single/multiple spacecraft measurements, Haaland et al. (2014) discussed the
157 dawn-dusk asymmetry at the flanks and at the dayside MP. Similar results were also re-
158 ported by Haaland et al. (2019), as observed by two of the THEMIS spacecraft, showing
159 the magnetopause being thicker on dawn ($\sim 14\lambda_i$, λ_i being the ion inertial length) than
160 on dusk ($\sim 8\lambda_i$), however no radial IMF conditions were included in the statistical study.
161 Additionally, other observations from INTERBALL-1 and MAGION-4 spacecraft revealed

162 asymmetry and deformation at the turbulent magnetopause (Šafránková et al., 2000). Us-
163 ing Geotail observations for northern and southern IMF, Wang et al. (2006) thoroughly
164 discussed the dawn-dusk asymmetry in ion density and temperature based on equatorial
165 distribution of plasma sheet ions.

166 To interpret the magnetopause motion and the dawn-dusk asymmetry, many sophisti-
167 cated models have been utilized, ranging from MHD to hybrid simulations. Early theoretical
168 studies showed a contrast of 10%-20% between dawn and dusk bulk plasma properties (e.g.,
169 Němeček et al., 2002; Walsh et al., 2012), however; those MHD-based models do not explic-
170 itly resolve kinetic effects, particularly at the foreshock region. For instance, using a global
171 hybrid model (kinetic ions and fluid electrons), Blanco-Cano et al. (2009) studied radial
172 IMF ($\theta_{vB} = 0$) impact on the solar wind interaction with the Earth's magnetosphere. The
173 study focused on the micro-physics processes and wave-particle interactions in the foreshock
174 region but briefly mentioned the dawn-dusk asymmetry issue. Three other models i.e. hy-
175 brid, Hall-less and Hall-MHD simulations have been tested in one study by Karimabadi et
176 al. (2004) for the analysis of MR regimes with the conclusion that dawn-dusk asymmetry
177 is obtained and should be related to ions flow. Recently, Turc et al. (2020) used the hybrid
178 -Vlasiator 2D-3V code to study asymmetries in the Earth magnetosheath for different IMF
179 conditions. For reference, the Vlasiator code provides a kinetic description of ions, solv-
180 ing directly the Vlasov equation for the particle distribution function in 2D-3D space, but
181 assumes a fluid description for electrons (e.g., Palmroth et al., 2018). The authors report
182 asymmetries larger than observed for the magnetic field strength, the plasma density, and
183 bulk velocity, a discrepancy that was attributed to using a single set of upstream conditions
184 in their simulations. It is interesting to remark that those authors obtained a stronger asym-
185 metry for magnetic field strength when IMF gets closer to the radial configuration. However,
186 it was not clear how the 2D spatial assumption and the fluid description of electrons in their
187 simulations affected the reported magnetosheath asymmetries.

188 Based on the discussion above, two important questions appear: 1) what happens to
189 the magnetopause shape, size, and location if flow-aligned IMF is applied to the system
190 when kinetic effects are included for all species? and 2) does this generate asymmetry in
191 the dawn-dusk and south-north directions so in the dayside magnetosphere?

192 To answer these questions, we undertake a modeling study utilizing IAPIC, a particles-
193 in-cell code (discussed in section 2). Our strategy is to be able to follow ions and electrons
194 self-consistently with the Maxwell equations describing the fields. Thus the full range of
195 collisionless plasma physics is captured for the macro-ions and macro-electrons involved in
196 IAPIC, yet with limitations due to the grid spatial resolution and assumptions made on the
197 plasma properties (particles density, ion/electron mass ratio, etc.) that we carefully discuss
198 in section 2 (see Blanco-Cano et al., 2006; Eastwood, 2008; Jacobsen et al., 2009; Brackbill,
199 2011; Masters et al., 2013; Ben-Jaffel & Ballester, 2014; S. Baraka, 2016). We adopt the
200 initial and the boundary conditions reported in (Suvorova et al., 2010; Samsonov et al.,
201 2017), we used single physical units for each parameter that were used in CCMC reported
202 in (Samsonov et al., 2017).

203 This paper is structured as follows. This section has introduced the impact of radial
204 IMF orientation on the dynamics of the Earth's magnetosphere and presented a brief survey
205 of observations of asymmetry in planetary magnetospheres. Two IMF orientations, namely,
206 radial IMF ($B = B_x$, 0° cone angle) and non-radial IMF ($|Bz| < |Bx| < |By|$, $\sim 50^\circ$ cone
207 angle) will be covered in the current study.

208 In section 2, we describe the IAPIC code in detail. The scaling of plasma parameters is
209 also presented and tabulated. In section 3, we show our findings regarding the magnetopause
210 motion and the magnetosheath asymmetry, an opportunity to compare to previous modeling
211 results and observations. In section 4, we discuss in detail the impact of the purely and non-
212 radial IMF on the dynamics of the Earth's magnetosphere, in light of the results obtained
213 so far. In section 5, we present a summary of our findings and future related work.

2 Initial conditions and Simulation Model: IAPIC

2.1 Simulation Model: IAPIC

We use the Institut d’Astrophysique de Paris-Particle-In-Cell EM 3D global code (IAPIC) for treating the plasma kinetically. IAPIC has previously been applied to simulate various magnetospheres in the solar system (S. Baraka & Ben-Jaffel, 2011; Ben-Jaffel & Ballester, 2013, 2014; S. Baraka, 2016). IAPIC handles the equations of motion for a large number of macro-particles (macro-ions and macro-electrons) self-consistently under the direct impact of electromagnetic fields through Lorentz force law (S. Baraka & Ben-Jaffel, 2007; Artemyev & Zelenyi, 2012).

The code was originally written by (Buneman et al., 1992), which used the boundary conditions reported in (Lindman, 1975) and charge conserving conditions as described in (Villasenor & Buneman, 1992). We use physical units for each parameter from (Samsonov et al., 2017) and scaled them to IAPIC values using a transformation matrix to convert GSM coordinates to the IAPIC code coordinates (see Fig. 1) as reported in (Cai et al., 2003). The solar wind parameters are tabulated in Table 1 for radial IMF and Table 2 for non-radial IMF (see also, Table 1, Cai et al., 2015).

We follow the evolution of the fields and particles within a $61 \times 45 \times 45 R_E$ domain with Earth centered and $20 R_E$ downstream of the sunward (inlet) side (Table 1). We chose time step $t = 3700 \Delta t$ as our comparison point which corresponds to 24 minutes of real time (approximately twice the SW transit time) after starting the simulation. Each time step is equivalent to ≈ 0.38 sec and the spatial resolution of the code is $0.2 R_E$. We track 7.0×10^7 particle pairs, with an ion to electron mass ratio of 64.

Our solar wind parameters for both IMF orientations are given in Tables 1 and 2 for radial and non-radial IMF, respectively. The parameters are set such that a consistent initial conditions are validated before the code run starts, denoted as $t = 0 \Delta$, and at the step time,

239 where the current study is considered i.e. $t = 3700\Delta t$. These two tables are compared to a
 240 similar study by (Cai et al., 2015)

Step time	$t = 0\Delta t$		$t = 3700\Delta t$	
Species/Parameters	ions	electrons	ions	electrons
Thermal velocity, $V_{thi,e}$	0.025	0.1	0.06	0.41
Debye length, $\Delta_{i,e}$	0.8	0.4	1.48	1.35
Larmor radius, $\lambda_{i,e}$	44.95	0.7	11.51	1.31
Gyro-frequency $\omega_{ci,e}$	$3. \times 10^{-3}$	0.20	$2. \times 10^{-3}$	0.31
Plasma-frequency $\omega_{pi,e}$	0.03	0.25	0.04	0.30
Temperature, $T_{i,e}$	$1. \times 10^{-3}$	$2. \times 10^{-4}$	4.9×10^{-3}	4.09×10^{-3}
Gyroperiod	2094.4	31.4	1289.81	20.15
Inertial length $d_{i,e}$	16.6	2.0	13.23	1.65

Unitless values

Step time	$t = 0$	$t = 3700\Delta t$
Sound speed C_s	0.045	0.01
Alfvén speed v_A	0.050	0.06
Alfvén Mach number M_A	2.83	1.4
Sonic Mach number M_s	3.16	0.92
Magnetosonic Mach number M_{ms}	2.0	0.77

Loaded Simulation Box Information

grid size	$\Delta = 0.2R_E = \Delta x = \Delta y = \Delta z$
Time Step	$\Delta t = \Delta_x / \Delta_v = 7.08$
Simulation box size	$(305 \times 225 \times 255)\Delta$
# of pair-particles	7×10^7 ion/electrons pairs
Ion to electron mass ratio	64
Particle density	$n_i = n_e = 4 / \Delta^3$

Table 1. Solar wind parameters at the initial state and after $t=3700 \Delta t$ in the undisturbed solar wind for both ions and electrons for radial IMF.

Step time	$t = 0$		$t = 3700\Delta t$	
Species/Parameters	ions	electrons	ions	electrons
Thermal velocity, $V_{thi,e}$	0.025	0.1	0.04	0.39
Debye length, $\Delta_{i,e}$	0.8	0.4	0.87	1.15
Larmor radius, $\lambda_{i,e}$	26.26	0.4	6.85	1.12
Gyro-frequency $\omega_{ci,e}$	$5. \times 10^{-3}$	0.343	0.01	0.35
Plasma-frequency $\omega_{pi,e}$	0.03	0.25	0.04	0.34
Temperature, $T_{i,e}$	9×10^{-4}	$2. \times 10^{-4}$	2.18×10^{-3}	3.75×10^{-3}
Gyroperiod	1256.6	18.3	1153.15	18.02
Inertial length $d_{i,e}$	16.1	2.0	11.71	1.46

Unitless values

Step time	$\Delta t = 0$	$t = 3700\Delta t$
Sound speed C_s	0.045	0.08
Alfvén speed v_A	0.05	0.06
Alfvén Mach number M_A	2.83	1.23
Sonic Mach number M_s	3.16	0.99
Magnetosonic Mach number M_{ms}	2.0	0.77

Loaded Simulation Box Information

grid size	$\Delta = 0.2R_E = \Delta x = \Delta y = \Delta z$
Time Step	$\Delta t = \Delta_x / \Delta_v = 7.08$
Simulation box size	$(305 \times 225 \times 255)\Delta$
# of pair-particles	7×10^7 ion/electrons pairs
Ion to electron mass ratio	64
Particle density	$n_i = n_e = 4 / \Delta^3$

Table 2. Solar wind parameters at the initial state and after $t=3700 \Delta t$ in the undisturbed solar wind for both ions and electrons for non-radial IMF.

2.2 Initial conditions

In IAPIC, the spatial and temporal scales (mass ratio and charge to mass ratio, etc ...) are chosen in order to be able to regenerate MHD large-scale classical structure of the Earth's magnetosphere (e.g., Omidi et al., 2004). For their modeling, Samsonov et al. (2017) used MHD and Community Coordinated Modeling Center (CCMC) resources, while the observational data are obtained from ACE, THEMIS and WIND spacecraft. Samsonov

247 et al. (2017) studied the impact of non-radial IMF , using a cone angle threshold value of
 248 50° on the magnetopause size and shape. Contextually, in the current study, we used the
 249 physical parameters they used in their MHD initial conditions and scaled them to the IAPIC
 250 initial condition values not only for non-radial IMF (where B_x and B_y are dominant over B_z ,
 251 upper limit cone angle case of Samsonov et al. correspond to their threshold value), but also
 252 for purely radial IMF (where B_y and B_z are absent). The purely radial IMF is an additional
 253 case included to study differences and similarities with the non-radial nature of IMF on
 254 both magnetopause's shape and size and their role in creating dawn-dusk asymmetries. The
 255 initial conditions of Samsonov et al. (2017) and our two IMF orientations are then tabulated
 256 in Table 3.

Table 3. MHD initial conditions and their corresponding IAPIC scaled values for radial and non-radial IMF orientation(Samsonov et al., 2017).

Parameters	Physical Units		Code Units	
	MHD	IAPIC _{radial}	IAPIC _{non-radial}	
N_{SW} (n/cc)	2.606	4.	4.	
T_{sw} (Kelvin)	32263	5×10^{-4}	5×10^{-4}	
V_x (km/s)	-470.69	0.1412	0.1412	
V_y (km/s)	-7.80	0	0	
V_z (km/s)	-5.09	0	0	
IMF _x (nT)	-2.2	0.25	0.25	
IMF _y (nT)	2.99	0	-0.34	
IMF _z (nT)	0.659	0	0.075	
Tilt angle	31°	31°	31°	
Initial Cone Angle(θ_{Bx})	54°	0°	54°	
Initial Clock Angle(θ_{CA})	77.6°	Undefined	77.6°	

3 Simulation Results

To our knowledge, a full 3D global kinetic modeling of radial IMF impacts on the dynamics of the magnetosphere has not been published, though the backstreaming of ions in the solar wind flow has been theoretically discussed (e.g., Willis, 1978, Eq. 3). The non-radial IMF event on July, 16th, 2007 observed by the THEMIS probes was chosen because it has been the subject of several detailed studies (Jelínek et al., 2010; Suvorova et al., 2010; Samsonov et al., 2017). The solar wind parameters and initial conditions were scaled for IAPIC as described in section 2. For purposes of comparison, we discuss in detail the plasma properties at the time step $3700\Delta t$ of our simulation for both purely radial and non-radial IMF (IMF orientation corresponding to the threshold cone angle value $\simeq 50^\circ$ used by Samsonov et al. (2017) as described in the introduction). This time step corresponds to ≈ 24 minutes of real time, a relatively long enough period to perform a kinetic simulation of the dayside magnetosphere. In the following, IAPIC simulation results are analyzed to determine the magnetopause shape, size and location for the two IMF conditions considered, which give us a good frame to characterize any dawn-dusk asymmetry in the system.

3.1 Magnetopause response to radial and non-radial IMF

We derive the magnetopause's size from the location of the vertical cut of the maximum density gradient steepening using the number density derivative to get the maximum steepening (e.g., Garcia & Hughes, 2007; J. Lu et al., 2015).

We also use the pressure balance method to derive the MP location, a technique that offers an opportunity to explicitly include kinetic effects. Basically, in the pressure balance method, the dynamic and thermal pressures counterbalance the dipole magnetic pressure. Because of the magnetic field axis tilt -31° at the time of THEMIS observation, the system is inherently asymmetric and the Cartesian grid used in the IAPIC simulations is not adequate to accurately derive a density gradient in most planes, particularly in the tilted magnetic equatorial plane. To overcome this difficulty, we transform our Cartesian 3D sim-

283 ulation box quantities (density, velocity vector, . . . etc, at (x,y,z) positions) into a spherical
 284 3D domain (same quantities at (r, θ , ϕ) positions), at the price of losing data from regions
 285 outside a spherical volume of radius equal to the smallest dimension of the initial Cartesian
 286 box (the Dusk-Dawn and South-North in our case). Our study does not suffer for that limi-
 287 tation because the dayside MP, our region of interest, is located inside the selected spherical
 288 domain. After checking that both reference frames provide the same spatial distribution of
 289 all physical quantities along the Sun-Earth (OX), the Dusk-Dawn (OY), and South-North
 290 (OZ) axis, we focus on deriving the magnetopause size at two key planes, namely the tilted
 291 magnetic equatorial plane $\theta = -31^\circ$ and the plane $\theta = 0^\circ$ that contains the Sun-Earth line.
 292 To quantify the MP expansion, we inject our initial solar wind conditions in physical units
 293 into the Shue model (Shue et al., 1997), which leads to a MP size equals to $10.3 R_E$. There-
 294 fore, this MP size will be used as the reference in the current study. Our findings are
 295 summarized and tabulated in Table 4.

296 To better visualize asymmetries on large scales of the system, we introduce various
 297 contour plots that show a 2D cut of the plasma density distribution and magnetic field
 298 topology in 3 planes as shown in Fig. 2 and 3. The dipole field tilt of (-31° , North summer)
 299 seemingly has an impact on the macrostructure of the magnetospheric dynamics. Fig. 2a-
 300 c (d-f) show the 2D contour plots for plasma distribution along the Sun-Earth axis, the
 301 Dusk-Dawn axis, and South-North axis for radial IMF (for non-radial IMF).

302 Fig.2a&d clearly show the (-31°) tilt angle between the Sun-Earth axis (OX) and the
 303 magnetic equator axis for radial and non-radial IMF, respectively. Therefore, the forefront
 304 of the solar wind coplanar inflow approaches the planet and hits the upper boundary of the
 305 magnetosphere before it comes in head-on combat with the magnetic equator axis. This
 306 results in squeezing the magnetopause at high latitude and relaxes it in lower latitude.
 307 This torque-like effect generates plasma streaming that has a flare out configuration for
 308 radial IMF and a confined configuration for non-radial IMF as in Fig. 2d. For both IMF
 309 orientations, localized density maximas (yellow areas) can be seen at the subsolar point

310 (stagnation region) close to OX although being extended southward for the non-radial case.
 311 These regions extend azimuthally duskward for both IMF orientations (Fig. 2b&e). Also,
 312 large denser regions are present near the north cusp for both orientations although a smaller
 313 one can be seen near the south cusp too for the non-radial case. In the linear plot Fig. 8, it is
 314 seen like a hump at $\approx -16R_E$ along the Sun-Earth line for non-radial IMF. We do not know
 315 why this layer appears for non-radial but not for radial IMF. The relaxation of the southern
 316 part of the magnetosphere showed a denser plasma population up to $30R_E$ tailward and
 317 flared in toward north at around $25R_E$ for non-radial IMF in Fig. 2d. The cavity around
 318 the planet position is smaller and more confined in the non-radial IMF case than in the radial
 319 IMF case. Moreover, Fig. 2b&e show the equatorial plane plasma distribution for radial and
 320 non-radial IMF, respectively. Particle entry inside the magnetosphere is largely distributed
 321 around the planet making the cavity reaches $\pm 5R_E$ along the Dusk-Dawn direction and
 322 around $3R_E$ tailward, with plasma tube along the Sun-Earth line up the planet position.
 323 On the other hand, the effect of B_y for the non-radial IMF in Fig. 2e, shows that the
 324 magnetopause is compressed on both dusk and dawn sides. The cavity around the planet
 325 is more confined and reduced in size to $\pm 5R_E$ along South-North direction for radial IMF,
 326 and $\pm 4R_E$ for non-radial IMF, respectively (Fig. 2c&f). The plasma density in the South-
 327 North/the Dusk-Dawn plane for radial IMF (Fig. 2c) shows denser plasma in the dusk sector
 328 from -10 to -20 R_E than in the dawn sector from 10 to 20 R_E , while in the northern sector
 329 there is a denser plasma that extends from around 10 to 17 R_E but not regularly structured
 330 with same thickness in the southern sector. It appears that there is a finger-like structure
 331 (particle entry, small blue region) at around $-5R_E$ on the duskside that has an extension
 332 of about $1R_E$ in the cavity around the planet. On the other hand, for non-radial IMF the
 333 plasma distribution contour shows smaller cavity size and also a denser plasma on the dusk
 334 side(Fig. 2f).

335 Fig. 3 shows the corresponding magnetic field lines topology of plasma density contour
 336 shown in Fig. 2, respectively. This figure sheds light on the differences and similarities be-
 337 tween two IMF orientations along three different planes.

338 In Fig. 3a, the radial IMF field lines along OX are horizontal at $-20R_E$ and $\pm 3R_E$ along
 339 South-North direction and seen curled at $\pm 10R_E$. At the magnetopause position, the field
 340 lines divert at $f(x,z)=(-10,-8)R_E$. On the dayside magnetosphere, there are two potential
 341 lobe magnetic reconnection sites(MR) sites. They are approximately located in the south-
 342 ern hemisphere at $f(x,z)=(0.5,-12)$ and at $(-7.6,11.9)R_E$ in the northern hemisphere. The
 343 magnetic field line topology shown in Fig. 3d is horizontal in the undisturbed SW; this
 344 was not the case in Fig. 3a. This difference is attributed to the impact of B_y . In Fig. 3d
 345 potential lobe MR sites are seen also at $f(x,z)=(-8,-12)$ in the southern hemisphere and
 346 at $(5,15)R_E$ in the northern hemisphere. Constant attention should be made when looking
 347 at Fig. 3b, taken in the equatorial plane, because of the dipole tilt, what is shown here
 348 for radial IMF is the high latitude magnetopause along OX in the Dusk-Dawn direction.
 349 It is found that field lines from IMF connect to dipole field and permit particle entries at
 350 that latitudes. The wavy structure in the night-side (not the focus of the current study)
 351 indicates a complex current system induced at that distance. A potential MR site is shown
 352 at $f(x,y)=(-7.6,9.9)R_E$. The curling of magnetic field lines at $f(x,y)=(5,-15)$, $(-15,-7)R_E$
 353 corresponds to the plasma dynamics shown in Fig. 2d. Same in Fig. 2e for non-radial IMF,
 354 the curled magnetic field lines at a latitude corresponding to $\approx 6R_E$ (north) are directed
 355 toward dusk-midnight direction. Potential MR sites are at $f(x,y)=(4.4,5.9)$, $(-8.6,0.1)$, $(3.5,-$
 356 $7.9)R_E$. In Fig. 3c, the magnetic field topology shows a more extended structure of closed
 357 magnetic field lines for both duskside and dawnside than the non-radial case. The regions
 358 extends until $\approx \pm 14R_E$ along the dusk-dawn axis and reach up $\pm 12R_E$ along the south-
 359 north axis. In contrary, Fig. 3f shows different structures, where the extension of field lines
 360 is less important along the dusk-dawn axis due to large scale connections of planetary and
 361 interplanetary magnetic field lines and clear MR sites located in the southern hemisphere on
 362 both dusk and dawn sides at $f(y,z)=(-12.5,-2.6)$, $(14,-3)R_E$, respectively. Such reconnection
 363 sites are not present (at least in this plane) for the radial case. The detailed investigation of
 364 the MR regions is out of the scope of the present study yet these results suggest that these
 365 reconnection regions are formed in the northern and southern lobe regions and extend to

366 the dawn and dusk flanks. They could lead to the squeezing of the dusk and dawn flanks of
 367 the magnetopause seen in Fig. 2e.

368 In the first step, we focus on the direction defined by $\phi = -180^\circ$ in both planes.
 369 Using the maximum density steepening technique, we derive comparable values for the
 370 magnetopause position at (~ 10.6 , ~ 11.0) R_E , respectively for radial and non-radial IMF
 371 along the Sun-Earth axis. We also obtain the same size when the effect of backstreaming
 372 ions is removed (by post-processing) from the bulk flow for both IMF orientations. It would
 373 suggest as it will be confirmed below that while the contribution of the backstreaming ion
 374 population to the total density is small and does not change the location of the density
 375 gradient maximum their contribution to the total pressure is important. In particular,
 376 finite Larmor radius effects are more important for energetic ions. Along the tilted magnetic
 377 equatorial axis, the magnetopause positions are (11.6, 12.0) R_E with bulk flow, which also
 378 remain unchanged without backstreaming ions, respectively for the two IMF conditions.

379 First, we note that the different magnetopause positions derived from the IAPIC simu-
 380 lation are all larger than the expected magnetopause position ($\sim 10.3 R_E$) derived from the
 381 Shue model (Shue et al., 1997). We remind that this reference MP size corresponds to the
 382 initial solar wind physical parameters used in our simulations. All values derived show a
 383 sunward expansion of the magnetopause position along the two selected axes. The magne-
 384 topause appears to be subjected to a reduced SW dynamic pressure that allows the dipole
 385 magnetic field network to expand outward. Based on the maximum density steepening tech-
 386 nique, it is remarkable that our model predicts the magnetopause expansion self-consistently
 387 in the range (0.3-1.3) R_E along the Sun-Earth axis and tilted magnetic equatorial axis for
 388 the radial IMF case but also (0.7-1.7) for the non-radial IMF, respectively.

389 In the following, we explore our 3D IAPIC simulation results to try to uncover potential
 390 processes that could be at the origin of the measured expansion. Since early reports, several
 391 studies pointed to the potential impact of kinetic effects, particularly with the detection of
 392 the signature of particles streaming in a direction opposite to the solar wind (Spreiter &

393 Alksne, 1969; Willis, 1978; Sibeck et al., 2001; Samsonov et al., 2017). As IAPIC simula-
 394 tions offer the access to all populations of particles (macro-particles) with specific kinetic
 395 properties, we tried to extract those particles on the dayside that move sunward, against the
 396 main impinging solar flow. That statistical sub-population of particles has its own kinetic
 397 properties and most importantly counterbalances the ram pressure of the incident solar
 398 flow, as if it was originating from the magnetosphere and flowing outward. It is important
 399 to stress that this population has kinetic properties (temperature, speed, etc.) much dif-
 400 ferent from the planetary ionospheric population that flows from the plasmasphere or the
 401 polar wind, In Fig. 4, bulk pressures (dynamic, thermal denoted P_{dyn} and P_{thm} , respec-
 402 tively) are shown with and without taking into account the contribution of backstreaming
 403 ions to highlight the difference they make in the pressure balance. First, we remark that the
 404 thermal pressure is dominant over dynamic pressure in the magnetosheath as expected for
 405 a conversion of the convective flow energy to thermal energy after the bow-shock crossing.
 406 P_{dyn} and P_{thm} cross P_{mag} at two points, i.e. with and without backstreaming ions included.
 407 The corresponding size of the MP is $\sim 10.8R_E$ for radial IMF and $\sim 11.7R_E$ for non-radial
 408 IMF along the Sun-Earth axis. Importantly, if the backstreaming ion effect is removed,
 409 then the magnetopause size drops down to 10.5 and $11.4R_E$ for the same IMF orientations,
 410 respectively. The magnetopause is also measured along the tilted magnetic equatorial axis
 411 with and without backstreaming ions and found equal to 11.9 , $11.5R_E$ for radial IMF and
 412 12.0 , $11.6R_E$ for non-radial IMF, respectively. To summarize, these findings are tabulated
 413 in Table 4. It is worth noting that the expansion ranges when using the pressure balance
 414 method for deriving the MP size is slightly different from that using the density steepening
 415 method. For example, the MP expansion rate is 0.5 - $1.4R_E$ for radial and non-radial IMF
 416 along the Sun-Earth axis, compared to 0.3 - $0.7R_E$ derived by maximum density steepening
 417 method. The difference between the two measurements is 0.2 - $0.7R_E$. The expansion range
 418 is 1.6 - $1.7R_E$ as derived by pressure method compared to 1.3 - $1.7R_E$ as measured by density
 419 steepening method, respectively along tilted magnetic equatorial axis. With only a differ-
 420 ence between the two methods of $0.3R_E$ for radial IMF and similar values for non-radial IMF

421 along the tilted magnetic axis. Surprisingly, both methods suggest that the magnetopause
 422 expansion at the subsolar point is larger for the non-radial case than for the radial case. It
 423 is probably the effect of the diffuse backstreaming ions in the case of non-radial IMF which
 424 are hotter than that of radial IMF which explains the expansion toward the sun as well, as
 425 a reference is the cross-field diffusion discussed in (Tsurutani & Lakhina, 1997; Paschmann
 426 et al., 1981). We emphasize that the ring current that generates the dipole field for both
 427 radial and non-Radial IMF is the same. That's to say, the solar wind conditions, and the
 428 dipole strength are the same for both IMF cases, except for the non-radial IMF, where B_y
 429 is dominant over B_x and B_z . Therefore, any noticeable differences such as the larger MP
 430 expansion is directly related to the presence of the IMF B_y . It is worth to continue broadly
 431 investigating the radial IMF by PIC code to better understand the related physics that
 432 handle this problem.

Maximum Density Steepening magnetopause derivation

IMF /Axis	The Sun-Earth Axis		Tilted Magnetic equator axis	
	Yes	No	Yes	No
Kinetic effect	Yes	No	Yes	No
magnetopause for radial IMF	10.6 R_E	10.6 R_E	11.6 R_E	11.6 R_E
magnetopause for non-radial	11.0 R_E	11.0 R_E	12.0 R_E	12.0 R_E

Pressure balance magnetopause derivation

IMF/Axis	The Sun-Earth Axis		Tilted Magnetic equator axis	
	Yes	No	Yes	No
Kinetic effects	Yes	No	Yes	No
magnetopause for radial IMF	10.8 R_E	10.5 R_E	11.9 R_E	11.5 R_E
magnetopause for non-radial	11.7 R_E	11.3 R_E	12. R_E	11.6 R_E

Table 4. Summary of results for the MP location is tabulated as derived by density steepening method (derivative of number density) and pressure balance methods for both IMF orientations. The values are measured on both the Sun-Earth Axis and tilted magnetic equatorial axis. The kinetic effect is when the bulk flow (including backstreaming ions) is considered, and its absence when inflow (earthward) only is considered. The reference size for these values is $10.3R_E$.

433 In their papers, Bonifazi and Moreno (1981b, 1981a) used ISEE2 data of 3253 ion
 434 spectra that correspond to ≈ 90 hours, studying the density and energy of the backstreaming
 435 ions. They quantitatively characterized them into three categories. The authors used a
 436 scaling factor such that the ratio (A) of the backstreaming bulk speed over their thermal
 437 speed to identify the following three populations: ≥ 1.2 for reflected ions, ≤ 0.8 for diffuse
 438 ions and an intermediate population $0.8 \leq A \leq 1.2$.

439 Here, we adopted their method to quantify the characteristics of the backstreaming ions
 440 in the dayside solar wind flow. First, a simple statistical study of the dayside populations
 441 shows that the solar wind bulk flow is composed by 16.5% and 20% of backstreaming ions
 442 for radial and non-radial IMF, which confirms that their contribution to the total density is
 443 small whereas its contribution to the total pressure can be crucial. Fig. 5a shows that, for
 444 radial IMF 72.5% of backstreaming ions are characterized as reflected ions and only 27.5%
 445 as intermediate ($0.8 < A < 1.2$). For the non-radial IMF case, we found a totally different
 446 characteristics for backstreaming ions. There are only identified as 21.6% reflected particles,
 447 31.4% intermediate particles and 47.0% diffuse particles along the same OX axis. To follow
 448 up the impact of the tilted magnetic axis on the particles populations, we also conducted
 449 the same statistical analysis on the tilted magnetic equatorial axis. We found for radial
 450 IMF that 59% of ions are reflected and 41% are in the intermediate phase. On the other
 451 hand, backstreaming ions are characterized as 23.5% of reflected ions, 53% of intermediate
 452 case, and finally 23.5% for diffuse ions for non-radial IMF. In Fig. 5 we found that for radial
 453 IMF, on both axis, most of the backstreaming ions are in the reflection mode, with a small
 454 percentage in intermediate mode at the bow shock. On the other hand, for non-radial IMF,
 455 on both axis, backstreaming ions are in intermediate and diffuse mode in the solar wind,
 456 but the reflection mode appears to be dominant around the bow shock.

457 Still, to better understand the kinetics of the distribution of the backstreaming ions,
 458 we show in Fig. 6 the velocity distribution function (VDF) of solar wind ions along the
 459 Sun-Earth line as far as $-20R_E$. For the purely radial IMF case, a substantial fraction

of VDF spatial distribution of backstreaming ions is found in the three planes (XZ, XY and YZ) whereas only a small fraction is obtained for non-radial IMF, especially in the YZ plane. The VDF in Fig. 6a shows the reflection of the plasma sunward and southward for radial IMF, with minor reflection for non-radial IMF but larger distribution toward north and earth direction as confirmed by Fig. 5. It is also found that at $Y=Z=0$ and $X=-20R_E$ that the reflection of backstreaming ions are larger for radial than non-radial IMF. While on the other hand in Fig. 6c&f, the spatial distribution of ions is reflected mostly toward the south and sunward for radial and mostly toward north for non-radial IMF.

In the following, we track the magnetopause shape for both IMF orientations in two different locations. In order to handle the complex geometry of the tilted dipole, we use spherical coordinates such that $\phi=-180^\circ$ at the dayside standoff distance ($\theta=0$) along the Sun-Earth Axis and ($\theta=-31$) along the tilted magnetic equatorial axis. In that frame, we track the shape every 20° along ϕ in two different axes. The MP shape for the two IMF orientations is constructed in the XY-plane and in the magnetic equator that both contain the dusk-dawn direction. In Fig. 7, the MP is shown in the half-plane that contains dawn (positive Y), so that the asymmetry between dusk and dawn clearly appears using a mirror image of the MP shape in the dusk half-plane that is over-plotted on the dawn half-plane. For example for the radial case, Fig. 7a&b show a small the dusk-dawn asymmetry for the two selected planes (i.e. XY and tilted magnetic equator planes) whereas this asymmetry is more important in the non-radial case; the duskside magnetopause being more extended than the dawnside (Fig. 7c&d).

In particular Fig. 7c, the MP along the Sun-Earth axis is squeezed earthward on the dawnside down to $7.5R_E$ whereas the dusk sector spreads out to $\approx 12R_E$. In Fig. 7d, we have a peculiar non-symmetric MP shape in the magnetic equator with a size $\approx 10R_E$ except near the Y-axis. In Fig. 8, the linear densities for both IMF orientations are plotted in three different directions. For purely radial IMF (Fig. 8a&b, ion and electron densities are over-plotted along the Sun-Earth line (upper panel $OX, Y=Z=0$) from -20 to $-10R_E$, the

487 Dusk-Dawn line (middle panel OY, X=-13, Z=0) from -20 to +20, and South-North line
 488 (lower panel OZ, X=-13, Y=0) measured. Densities in OY, and OZ panels are aimed to show
 489 the density profile just outside the MP position taken at $-13R_E$. The vertical dashed line
 490 in the upper panel shows where the densities are plotted in the other two directions. Fig. 8
 491 shows the quasi-neutrality of the solar wind, magnetosheath and magnetospheric plasmas.
 492 Ion and electron densities are correlated with no charge separation. Also, it is found that
 493 along the Dusk-Dawn axis and South-North axis taken just outside the MP there is an
 494 apparent asymmetry at both the dusk-dawn and south-north directions. For both IMF
 495 orientations, magnetosheath densities are larger on the duskside than on the dawnside and
 496 larger in the southern hemisphere than in the Northern.

497 For the non-radial case (Fig. 8b), we notice a hump/heap just upstream of the bow
 498 shock position at $\approx -16R_E$. We tracked backstreaming ions at that distance and only a little
 499 fraction was found. Its type corresponds to reflected ions according to the characterization
 500 of backstreaming ions reported in Fig. 5. The plasma jump at $X = -16R_E$ reaches factor 2.
 501 The same value is found when we perform a cut along OY and OZ at $X=-16 R_E$ (not shown)
 502 indicating that this jump is at a large scale and present across the full magnetosheath. The
 503 other major components of the solar wind dynamics is related to the ion velocity modulus
 504 that is shown in Fig. 9 in the same order. The density hump in Fig. 8b corresponds to a
 505 velocity decrease in Fig. 9b.

506 The temperatures of solar wind particle species are important to identify boundary
 507 crossing, for instance, between the cold component of the solar wind and the hotter com-
 508 ponent of the magnetosheath plasma. Furthermore, ion-to-electron temperature T_i/T_e is
 509 approximately conserved at the MP boundary (Wing et al., 2014). The T_i/T_e ratio in the
 510 magnetosheath was thoroughly investigated by Lavraud et al. (2009). In the current paper,
 511 the (T_i/T_e) ratio of the impinging solar wind is depicted in Fig. 10. For radial IMF Fig. 10a,
 512 T_i is slightly fluctuating in the solar wind until it increases by a factor 2 between -15 to
 513 $-12 R_E$ along OX as expected due to the shock crossing which slows down and heats the

514 plasma; then it decreases downstream before it increases again in the magnetosheath until
 515 it reaches the MP position. While on the other hand, the electron temperature T_e in the
 516 magnetosheath maintains a constant value and has increased by a factor 1.2 compared with
 517 the electron temperature in the solar wind. The average (T_i/T_e) ratio in the magnetosheath
 518 is ≈ 1.72 . The temperature profile for the non-radial IMF case shown in Fig. 10b is different
 519 from the purely radial IMF case. T_i starts constantly increasing at $-15R_e$ including the bow
 520 shock and the magnetosheath. From the solar wind to the magnetosheath, T_i increases by a
 521 factor 4. On the other hand, T_e starts increasing at $-16R_E$ and keeps rising through the mag-
 522 netosheath. The average (T_i/T_e) ratio in the magnetosheath is ≈ 1.1 . The ion-to-electron
 523 temperature ratio is discussed more in detail in section 4

524 The temperature anisotropy was studied extensively in the past (Gingell et al., 2015;
 525 Karimabadi et al., 2014; Treumann & Baumjohann, 2013). In the current paper, we were
 526 able to derive the temperature anisotropy of the solar wind particle species. Fig.10c shows
 527 for radial IMF, the average ion temperature anisotropy $T_{\perp i}/T_{\parallel i}$. In the dayside sector
 528 (between -18 and $-10 R_E$) this ratio is ≈ 2 . and inside the magnetosheath (between -14 and
 529 $-12.5 R_E$) it reaches 2.7. Therefore the perpendicular ion temperature anisotropy is stronger
 530 in the magnetosheath than in the solar wind. The maximum ratio is found at the bow shock
 531 ($\sim -14R_E$) with a factor of 3.3. The average electron temperature anisotropy $T_{\perp e}/T_{\parallel e}$ in
 532 the dayside sector equals to ≈ 2.3 , which is almost the same as inside the magnetosheath.
 533 Fig. 10d displays for the non-radial IMF orientation, the anisotropy average for ions in the
 534 dayside sector (between -18 and $-10 R_E$ along OX). The $T_{\perp i}/T_{\parallel i}$ ratio ≈ 6 for ions and
 535 ≈ 1.8 for electrons. In the magnetosheath (between -14 and $-12.5 R_E$ along OX) $T_{\perp i}/T_{\parallel i}$
 536 ratio is 3.2 whereas electron temperature is quite isotropic. These results will be discussed
 537 in section 4.

3.2 Dawn-Dusk asymmetry in the dayside magnetosphere under the influence of radial and non-radial IMF

The large scale results reported above all indicate systematic asymmetries in the Dusk-Dawn and South-North directions for the two IMF orientations. In the following, we try to quantify those asymmetries, particularly in the Dusk-Dawn direction for the radial and non-radial IMF cases we have simulated. Figures 2b,c,e,f,7, and 8 visually show asymmetry in the Dusk-Dawn direction.

Fig. 2b,e show the Dusk-Dawn asymmetry along the Sun-Earth direction (OX) and Fig. 2c,f show the asymmetry along the Dusk-Dawn (OY) and South-North (OZ) directions. The linear density plots are shown in Fig. 8, middle panel, plotted along the dusk-dawn direction at $X \approx -13R_E$. The asymmetry in the South-North planes can be seen in Fig. 8 lower panel. In Fig. 11, some solar wind parameters i.e. N_i , V_i , and T_i , and Fig. 12 B_x , B_y and B_z are plotted along three different axes (parallel to OX) for each IMF orientation. Two of which are plotted at $Y = \pm 6R_E$ on both sides of OX axis, and the third along the Sun-Earth line from -18 to 10.8 and $11.7 R_E$ for radial and non-radial IMF. Dashed lines are the calculated positions of the MP at dawn and dusk ($Y = \pm 6R_E$, green and red dashed lines, respectively) and along OX ($Y = 0$, blue dashed line) as measured from the gradient density method (same as shown in Fig. 7).

In the magnetosheath, left to the vertical blue dashed line, all plasma parameters are asymmetric. On the dusk side (red dashed line), the MP position is located at -8.5 , and $-7.7R_E$ for radial and non-radial IMF. Whilst on the dawn side (green dashed line), it is located at -7 , and $-5.2 R_E$. For both IMF orientations, ion density increase in the magnetosheath is larger on the duskside than on the dawnside (Fig.11). The largest increase is along the symmetry axis (OX). For the radial case, ion velocity (V_i) decreases after the bow shock crossing along (OX) whereas this deceleration is less important for both dawn and dusk sides until reaching the magnetopause. For the non-radial case, the same behavior is shown along (OX) whereas the ion flow seems to accelerate until the magnetopause crossing on the

565 duskside and to decelerate on the dawnside even more than along (OX). Ion temperature
566 T_i in the solar wind and in the magnetosheath is larger on the dawnside for the radial case
567 whereas it does not show any the dusk-dawn asymmetry for the non-radial case. In Fig. 12,
568 for both IMF orientations, B_z becomes positive close to the magnetopause likely due to
569 the draping effect. Furthermore, the large initial IMF B_y of non-radial case (positive in
570 GSE, negative in IAPIC coordinates = -0.34) remains quite constant and homogeneous in
571 the solar wind and magnetosheath regions. For the radial case, the B_y component is more
572 variable and different between dusk and dawn side in the solar wind and magnetosheath
573 regions. Initial IMF B_x (negative in GSE and positive in IAPIC coordinates = 0.25) does
574 not remain constant and shows the Dusk-Dawn asymmetry. A large increase occurs only
575 in the dawn magnetosheath sector. For the non-radial case, B_x remains quite steady in the
576 dayside region but is larger on the duskside than along OX and on the dawnside where the
577 initial value has been reduced.

578 4 Discussion and Analysis

579 As described in section 3.1, we derived the MP position (10.6,11.0) R_E along the Sun-
580 Earth line for purely and non-radial IMF, respectively (using the location of the maximum
581 number density gradient). In addition, we have shown that PIC simulations offer the possi-
582 bility to isolate backstreaming ions from the pool of particles in the box simulation. This
583 process allows us to derive their contribution to the dynamic and thermal pressures in the
584 dayside magnetosphere. It is important to stress that other complex effects could be in-
585 duced by the presence of those backstreaming particles, like induced currents and fields, that
586 will be considered in a future study. Subtracting the contribution of backstreaming ions in
587 the ensemble average of the plasma properties increases the resulting system pressure and
588 consequently moves the magnetopause location toward Earth.

589 Using the balance between ram pressure and magnetic pressure (e.g., Willis, 1978, Eq.
590 3) we were able to derive the MP size in different planes with and without backstreaming

ions (Table 4). These calculations reveal the impact of backstreaming ions in reducing the solar wind dynamic pressure allowing for MP expansion by $0.3-0.4R_E$. All our findings above also suggest the important results that by neglecting ions kinetic effects, MHD simulations implicitly overestimate SW pressure in the dayside region and underestimate the MP size.

For instance, the MP expansion range derived here is consistent with the expansion observed by THEMIS spacecraft for the event of 16 July 2007. To get the observed expansion with their MHD model, Samsonov et al. (2017) were forced to modify the solar wind properties, propagated from WIND and ACE *in situ* measurements, of their boundary conditions. This means that a non-negligible fraction (up to $\sim 40\%$) of the observed expansion that is due to backstreaming particles was modeled in their study by an ad hoc reduction of the SW dynamic pressure.

We conclude that the dynamic pressure of backstreaming ions contributes significantly to the expansion/compression of the magnetopause. Note that when the magnetopause is derived from the density maximum steepening, the effect of the backstreaming ions is not significant as their contribution to the total density is small. This indicates that the main driver of the expansion of the magnetopause is the upstream reduction of the solar wind dynamic pressure in the dayside region due to the reduction of the solar wind bulk flow by the presence of the backstreaming ions, which although being a small percentage of the total solar wind ion population (16.5% and 20% for radial and non-radial IMF, respectively) have a strong effect on the dynamic pressure. More generally, the insensitivity of the MP size to the density of backstreaming ions confirms the conclusions reported in (Samsonov et al., 2020, Eq. 2), that density and velocity (dynamic pressure) might have different contributions to the effective values of the dynamic pressure component in the pressure system balance used in driving the magnetopause position. This appears clearly in our results in Table 4.

However one can notice that for the non-radial case with a large positive IMF B_y component, the effect of backstreaming ions could have been expected to be more important on the dawnside where the foreshock region is moved leading to a pronounced magnetopause

618 expansion on the same side. Instead, we found that the magnetopause is moved earthward
619 in both dawn and dusk sectors. We suspect that this effect could be due to the formation
620 of magnetic reconnection regions across the dayside magnetopause seen in Fig. 3 in these
621 specific IMF conditions (with a clock angle of 77.6° , a cone angle of 54° and a large dipole
622 tilt of -31° corresponding to a North summer time) rarely investigated in past studies
623 (e.g., Trattner et al., 2007). Indeed, the dayside reconnection process is known to erode
624 the magnetopause therefore moving earthward the magnetopause boundary. Our results
625 could suggest that the reconnection process which erodes the magnetosphere could dominate
626 against the effect of the backstreaming ions which tend to expand the magnetopause. The
627 detailed investigation of the magnetic reconnection process in our simulations is out of the
628 scope of the present study and will be addressed in a further study.

629 Using THEMIS measurements, Wang et al. (2012) showed how the T_i/T_e ratio changes
630 in the magnetosheath and the plasma sheet. They showed that $T_i/T_e \approx 4 - 12$ in the
631 magnetosheath. In the tail plasma shee, this ratio spans $\approx 6 - 10$. Other studies statistically
632 examined the T_i/T_e in different regions in the magnetosphere to find a ratio $\approx 6-12$ close to
633 the magnetopause (Lavraud et al., 2009, and references therein) . On the other hand the
634 T_i/T_e ratio was as low as ≈ 3 at the magnetosheath flanks (Lavraud et al., 2009). In the
635 current paper, we show in Fig. 10a&b, the ion and electron temperature ratio T_i/T_e in the
636 dayside region. In the magnetosheath this ratio is found about 1.72 and 1.1 for radial and
637 non-radial IMF, respectively (Dimmock et al., 2014, 2015).

638 On the other hand, the presence of backstreaming particles should also affect the tem-
639 perature anisotropy in the dayside region ahead of the magnetosphere. Grygorov et al.
640 (2017); Samsonov et al. (2012) showed that the temperature anisotropy in the magne-
641 tosheath controls the pressure distribution near the magnetopause. Here we found that
642 the ion temperature anisotropy ratio is about 2 in the magnetosheath for radial IMF, and
643 about 6 for non-radial IMF (Fig.10c&d), consistent with Wang et al. (2012). Analysis of

644 the temperature distributions will be used in future work to study microinstabilities and
645 reconnection.

646 To characterize the kinetic properties of the backstreaming particles, we have first used
647 the nomenclature of Bonifazi and Moreno (1981b) and obtained results given in section 3.
648 In Table 5, we show the bulk speed of backstreaming ions in real physical units in accor-
649 dance with the characterization factor reported in (Bonifazi & Moreno, 1981b). It is found
650 that for both IMF orientations and along both axes, the magnitude of the bulk velocity
651 of the backstreaming ions (directed sunward) is larger than the full solar wind velocity.
652 Despite a relatively small percentage of the total ion population, backstreaming ions re-
653 duce significantly the solar wind velocity. Furthermore, thermal velocities of backstreaming
654 ions are larger for the non-radial case than for the radial case, suggesting that heating of
655 backstreaming ion is more important in the non-radial case.

656 The second major finding of this study is the Dawn-Dusk asymmetry. Uncovering
657 its origin is important for better understanding, modeling and prediction of space weather
658 phenomena (e. g., S. Lu et al., 2016). Asymmetry is observed by Cluster spacecraft in
659 north-south magnetotail planes (Haaland et al., 2017; Samsonov, 2006) and in dawn-dusk
660 planes (A. P. Walsh et al., 2014; Samsonov, 2011; Dimmock et al., 2017; Turc et al., 2020).
661 Both observations and numerical simulations have revealed that the magnetopause size is
662 a function of IMF strength and orientation, and solar wind dynamic pressure, which by
663 turn modify the magnetopause shape and generate dawn-dusk asymmetries (Liu et al.,
664 2019). Using data from IMP 8 and ISEE1, ISEE 3 and WIND, (e.g., Paularena et al.,
665 2001, Table 3) showed a significant dawn-dusk asymmetry in the Earth's magnetosheath
666 which is larger on the dawn side than on the dusk side, for all IMF orientation. They
667 also showed that the IMF orientation impacts density asymmetry in dawn-dusk direction.
668 Paularena et al. (2001) reported the same kind of asymmetry in different regions in the
669 dayside magnetosphere in the Sun-Earth and the Dusk-Dawn plane. In their recent study,
670 Turc et al. (2020) discussed the magnetosheath asymmetry in terms of IMF, solar wind

Total number of particles inside the simulation box

	Radial	non-radial
# bulk flow ions	5.38958×10^7	5.21372×10^7
# backstreaming ions	8.87744×10^6	1.07256×10^7
percentage	16.5%	20%

Backstreaming Ions Characteristics

	Radial		non-radial	
	OX	Tilt	OX	Tilt
reflected ions	72. %	58. %	22. %	24. %
intermediate ions	27. %	41. %	31. %	53. %
diffuse ions	1. %	1. %	47. %	23. %
$V_{bp}(km.s^{-1})$	373	392	294	346
$V_{thm}(km.s^{-1})$	254	255	321	332
$V_{sw}(km.s^{-1})$	287	254	233	248

Table 5. The ratio of backstreaming ions to bulk flow of the number density for both IMF orientations is shown in the upper panel. The backstreaming ions are characterized with three categories (see Fig. 5). Based on scaling factor ((Bonifazi et al., 1980)) the backstreaming ions are reflected, intermediate or diffuse. V_{bp} is the bulk flow of the backstreaming ions, V_{thm} , their thermal speed and their full solar wind velocity V_{sw} (including contribution of backstreaming ions) are shown in the lower panel for both IMF orientations along OX and Tilt axis. This data is measured at the dayside magnetosphere

671 density, velocity by using Vlasiator hybrid code (Palmroth et al., 2018). They found that
672 magnetic field asymmetry and density variability in the magnetosheath are stronger when
673 IMF tends toward a radial direction. Similarly, using IAPIC, the dawn-dusk asymmetry in
674 the magnetosheath and in the solar wind is investigated. In our work, the MP shape in Fig.
675 7, shows how asymmetric the dawn-dusk sides are. A result that is confirmed in Fig. 11,
676 and 12, IMF, density, temperature and ion velocity are tested at the the dusk-dawn flanks
677 asymmetry in the magnetosheath. In the magnetosheath (left to the vertical blue dashed
678 line) all plasma parameters are asymmetric which is consistent with recent results obtained
679 by Turc et al. (2020). Furthermore, for both IMF orientations, the magnetopause is more
680 extended on the duskside (red dashed line) than on the dawnside (green dashed line).

681 Finally, our analysis of the location, shape and size of the MP with the techniques
682 developed for that purpose, in addition to the ability to quantify plasma parameters in 3D
683 to track asymmetries in the dusk-dawn and south-north direction, our code is applicable to
684 planetary and exoplanetary magnetospheres. Furthermore, our findings can also contribute
685 to alternative methods for a better analysis of soft x-ray imaging of the magnetosphere
686 (Sibeck et al., 2018) in a complementary manner. This includes the MP, the cusp dynamics,
687 the magnetosheath that is related to density structure which can be deduced from soft x-ray
688 observation.

689 Most current support to the SMILE mission is based on MHD modeling (SMILE work-
690 ing group). In light of the results obtained so far (see Figs. 4 and 7 , and Tables 4), our global
691 3D electromagnetic kinetic code provides another point of view on the range of expected
692 boundary locations under various solar wind flux. An accurate estimation of those bound-
693 ary locations are key to interpret the X-ray signal that will be detected by SXI, the SMILE
694 X-ray detector. In addition, our simulations provide details about ions kinetic properties
695 locally and on global scales (eg. Fig. 8), an additional tool for coupling plasma properties
696 that will be detected by the light Ion Analyser (LIA) and large scale structure that will
697 imaged by SXI. In light of the results obtained so far, we propose IAPIC, as a global 3D

698 electromagnetic kinetic code to simulate the MP, the cusps, and the magnetosheath, which
 699 should enhance the science return of space missions like the CSA – ESA SMILE mission.

700 5 Summary and Conclusion

701 We have utilized a three-dimensional kinetic particle-in-cell code (IAPIC) to determine
 702 the size, shape and location of the Earth’s magnetopause with a dipole tilt of -31° (North
 703 hemisphere summer) in response to solar wind conditions of radial ($B=B_x$) and non-radial
 704 ($|B_z| < |B_x| < |B_y|$) IMF. These two IMF orientations cover the range of non-radial IMF
 705 with a cone angle between 0 and 50° as considered by Samsonov et al. (2017) related to
 706 a magnetopause crossing event recorded by the THEMIS mission on 16 July 2007. The
 707 simulations show sunward MP expansions and predict asymmetric magnetosphere for both
 708 IMF orientations.

709 Using a reference MP size ($10.3 R_E$) independently derived from (Shue et al., 1997)
 710 and based on our pressure balance calculations (Table 4), the findings of this study are
 711 summarized as follows:

- 712 1. For purely radial IMF, the MP expands from 10.3 to $10.8R_E$ for the full bulk flow.
 713 The expansion is limited to only $10.5R_E$ when the effect of the backstreaming ions are
 714 dropped from calculations along OX axis. In other words, 40% of the observed ex-
 715 pansion is due to backstreaming solar wind particles. Moreover, along tilted magnetic
 716 axis, the MP expansion is from 10.3 to 11.9 and 11.5 with and without backstreaming
 717 ion effect, respectively.
- 718 2. For non-radial IMF, the expansion is from 10.3 to 11.7 (along Ox) and to $12R_E$ (along
 719 tilted axis) for the full bulk flow. It is limited to only 11.3 (along Ox) and $11.6R_E$
 720 (along tilted axis) when backstreaming ions are not accounted for in the flow.
- 721 3. For non-radial IMF and full bulk flow (i.e., including the effect of backstreaming
 722 ions), the expansion rate is 1.4 and $1.7R_E$ along OX and tilted magnetic equatorial
 723 axis, respectively. These rates are comparable with the average expansion rate of

- 724 1.3-1.5 R_E reported from THEMIS observations (Jelínek et al., 2010; Suvorova et al.,
725 2010), without being forced to modify the input solar wind parameters as done by
726 MHD model (Samsonov et al., 2017).
- 727 4. The backstreaming ions contribution to the bulk flow is 16.5%, and 20% for radial
728 and non-radial IMF, respectively along the OX axis in the dayside magnetosphere.
- 729 5. When deriving the MP position using the maximum density steepening method, the
730 backstreaming ions (characterized and quantified in this study) do not impact the
731 measured size of the MP for both IMF orientations along both OX and tilted axis
732 since they represent only a small percentage of the solar wind plasma.
- 733 6. In contrast, when the magnetopause is derived using pressure system balance without
734 accounting the effect of backstreaming ions, the magnetopause expansion is reduced
735 by 0.3 – 0.4 R_E (Table 4).
- 736 7. The difference between magnetopause derivation using maximum density steepening
737 (Garcia & Hughes, 2007; J. Lu et al., 2015) and the pressure systems balance using
738 definition of dynamic pressure as in (e.g., Willis, 1978, Eq. 3) is consistent with the
739 conclusion drawn by (Samsonov et al., 2020) that density and velocity act differently
740 as a component of dynamic pressure in the pressure system balance. While the
741 energetic backstreaming ions have a small impact on the total density, they have a
742 significant contribution to the total dynamic pressure. In our study, we also considered
743 the effect of thermal pressure in the magnetosheath in the pressure balance.
- 744 8. At the subsolar point, the magnetopause expansion is larger for the non-radial case
745 than for the radial case (for both OX and tilted axes). However, in the non-radial case
746 both dawn and dusk magnetopause flanks are squeezed toward the Earth which could
747 be due to the reconnection process in these specific conditions (large IMF B_y , with a
748 clock angle of 77.6°, a cone angle of 54° and a large dipole tilt of 31° corresponding to
749 a North summer time) rarely investigated in past studies. The detailed investigation
750 of the magnetic reconnection process in such conditions is out of the scope of the
751 present work and will be carried out in a further study.

- 752 9. We present new results showing the magnetopause shape in spherical polar coordi-
 753 nates for the two IMF directions. This new technique along with the magnetopause
 754 derivations given in Table 4 and Fig. 4 enables us to anticipate the sizes, shapes
 755 and locations of magnetopause for all magnetized planets, including magnetized exo-
 756 planets. Additionally, this technique accounts for the backstreaming ion contribution
 757 to the data used to derive the magnetopause shape, a key information that is not
 758 available with other types of simulations.
- 759 10. The current study enabled us to derive the solar wind temperature anisotropy, thus
 760 paving a research road to study kinetic microinstabilities in the solar wind-magnetosphere
 761 coupling (see Figs. 10). In the dayside sector (between -18 and $-10 R_E$ along OX)
 762 for non-radial IMF, T_{\perp}/T_{\parallel} is large and equal ≈ 6 for ions and ≈ 1.8 for electrons.
 763 For radial IMF, T_{\perp}/T_{\parallel} equals to 2. and 2.3 for ions and electrons, respectively. The
 764 $T_{\perp e}/T_{\parallel e}$ ratio can be employed to predicts whistler waves generated by temperature
 765 anisotropy like those observed by MMS (e.g., Le Contel et al., 2016). Temperature
 766 anisotropy is known to have important effects on the magnetic reconnection process
 767 (e.g., Gingell et al., 2015).
- 768 11. For both IMF orientations, the magnetopause is found asymmetric: its expansion is
 769 larger on the duskside than on the dawnside.
- 770 12. In light of the results so far obtained, our findings are considered an additional and
 771 key modeling supports to future near-Earth exploration projects, in addition to outer
 772 planets' moons and magnetospheres. For example, the newly developed technique
 773 to map the MP shape and position, or the ability to track backstreaming ions and
 774 their characterizations and their kinetic impact on the plasma flow will contribute
 775 to deepen our understanding about the kinetic behavior of plasma in the solar wind
 776 magnetosphere coupling and the study of exoplanets magnetospheres.

777 Future Directions

778 Radial and non-radial conditions are relatively infrequent configurations of the IMF at

779 Earth, but closer to the Sun, the Parker spiral would favor more and more non-radial IMF
780 orientation (Chang et al., 2019). This suggests that radial IMF conditions are more common
781 at Mercury, which has recently been investigated by MESSENGER and will soon be visited
782 by the BepiColombo spacecraft. Furthermore, Mercury’s magnetosphere is much smaller as
783 the magnetopause standoff position is only at about $2R_M$ (R_M being the Mercury radius) and
784 the ion gyroradius is about the size of the planet. Finite Larmor radius effects are expected
785 to play an ever more important role than in the Earth’s case (e.g., Johnson et al., 2014; Paral
786 & Rankin, 2013). Mercury is therefore a natural laboratory for investigating radial IMF and
787 related kinetic effects and we will prepare simulations in advance of BepiColombo’s arrival
788 at Mercury. Planets even closer to their stars are common in the galaxy (NASA Exoplanets
789 Archive *doi* = 10.26133/NEA2), suggesting that, particularly around cooler M- and K-
790 type stars, radial IMF may be a common condition. This impacts the structure of their
791 magnetospheres and may influence the escape of planetary atmospheric and ionospheric
792 constituents over time. The kinetic aspect of our approach is particularly sensitive to the
793 dynamics of the bow shock, which may be highly variable in the neighborhood of a small
794 star (Cohen et al., 2015), potentially producing accelerated particles and observable radio
795 emissions (Cohen et al., 2018). One more issue that will be considered for near future work
796 is the impact of the magnetosphere-ionosphere-magnetosheath coupling on magnetopause
797 location. We have tracked in the past H^+ and O^+ ions outflow from the ionospheric origin
798 in the dayside magnetosphere (S. M. Baraka & Ben-Jaffel, 2015). IAPIC can also be used
799 to study the outflow of plasmasphere low energy ions.

800 **Acknowledgments**

801 This work is carried out using binary data generated by IAPIC, a pic code that is a mod-
802 ified version of the Tristan code that is available to the public through GitHub: [https://](https://github.com/ntoles/tristan-mp-pitp)
803 github.com/ntoles/tristan-mp-pitp. THEMIS, ACE, and, Wind data are available at
804 <http://amda.cdpp.eu/>. The used data for generating results is available at ([https://doi](https://doi.org/10.48392/bar-001)
805 [.org/10.48392/bar-001](https://doi.org/10.48392/bar-001)). S Baraka acknowledges the NIA NASA grant # NNX15AE05G

806 for supporting this research via the Living and Breathing Planet project. L. Ben-Jaffel
807 acknowledges support from CNES under project PACES. S. Baraka thanks IAP-CNRS for
808 using their computing resources facilities and generating the simulation data. Authors
809 thanks the anonymous reviewers for their critical review and their important remarks that
810 enhanced the quality of this paper.

Accepted Article

References

- 811 Akasofu, S.-I. (1991). Development of magnetospheric physics. *Magnetospheric Substorms*,
812 *64*, 3–9.
- 813 Akasofu, S.-I., Roederer, M., & Krimigis, S. (1982). Dawn-dusk asymmetry of the tail region
814 of the magnetosphere of saturn and the interplanetary magnetic field. *Planetary and*
815 *Space Science*, *30*(10), 1061–1063.
- 816 Artemyev, A., & Zelenyi, L. (2012, December). Kinetic Structure of Current Sheets in
817 the Earth Magnetotail. *Space Science Reviews*, *178*(2-4), 419–440. doi: 10.1007/
818 s11214-012-9954-5
- 819 Asbridge, J., Bame, S., & Strong, I. (1968). Outward flow of protons from the earth's bow
820 shock. *Journal of Geophysical Research*, *73*(17), 5777–5782.
- 821 Baraka, S. (2016, April). Large Scale Earth's Bow Shock with Northern IMF as Simulated
822 by PIC Code in Parallel with MHD Model. *Journal of Astrophysics and Astronomy*,
823 *37*(2), 1–16. doi: 10.1007/s12036-016-9389-6
- 824 Baraka, S., & Ben-Jaffel, L. (2007, June). Sensitivity of the Earth's magnetosphere to
825 solar wind activity: Three-dimensional macroparticle model. *Journal of Geophysical*
826 *Research (Space Physics)*, *112*, 6212. doi: 10.1029/2006JA011946
- 827 Baraka, S., & Ben-Jaffel, L. (2011). Impact of solar wind depression on the dayside
828 magnetosphere under northward interplanetary magnetic field. *Annales Geophysicae*,
829 *29*(1), 31–46. Retrieved from <https://www.ann-geophys.net/29/31/2011/> doi:
830 10.5194/angeo-29-31-2011
- 831 Baraka, S. M., & Ben-Jaffel, L. (2015). Magnetospheric dynamical and morphological
832 response to multi-species plasma supply from the ionosphere: New comprehensive 3d
833 pic simulation. *AGUFM, 2015*, SM23B–2552.
- 834 Ben-Jaffel, L., & Ballester, G. (2013, May). Hubble Space Telescope detection of oxygen in
835 the atmosphere of exoplanet HD 189733b. *Astronomy & Astrophysics*, *553*, A52. doi:
836 10.1051/0004-6361/201221014
- 837 Ben-Jaffel, L., & Ballester, G. E. (2014, April). Transit of Exomoon Plasma Tori: New
838 Diagnosis. *apjl*, *785*, L30. doi: 10.1088/2041-8205/785/2/L30
- 839 Berchem, J., Richard, R. L., Escoubet, C. P., Wing, S., & Pitout, F. (2016, January). Asym-
840 metrical response of dayside ion precipitation to a large rotation of the imf. *Journal*
841 *of Geophysical Research (Space Physics)*, *121*, 263–273. Retrieved from [https://](https://ui.adsabs.harvard.edu/abs/2016JGRA..121..263B)
842 ui.adsabs.harvard.edu/abs/2016JGRA..121..263B doi: 10.1002/2015JA021969
- 843 Blanco-Cano, X., Omid, N., & Russell, C. (2006). Macrostructure of collisionless bow
844 shocks: 2. ULF waves in the foreshock and magnetosheath. *Journal of Geophysical*
845 *Research: Space Physics (1978–2012)*, *111*(A10).
- 846 Blanco-Cano, X., Omid, N., & Russell, C. (2009). Global hybrid simulations: Foreshock
847 waves and cavitons under radial interplanetary magnetic field geometry. *Journal of*
848 *Geophysical Research: Space Physics*, *114*(A1).
- 849 Bobra, M., Petrinec, S., Fuselier, S., Claffin, E., & Spence, H. E. (2004). On the solar wind
850 control of cusp aurora during northward imf. *Geophysical research letters*, *31*(4).
- 851 Bonifazi, C., & Moreno, G. (1981a). Reflected and diffuse ions backstreaming from the
852 earth's bow shock 1. basic properties. *Journal of Geophysical Research: Space Physics*,
853 *86*, 4397–4404. doi: 10.1029/ja086ia06p04397
- 854 Bonifazi, C., & Moreno, G. (1981b). Reflected and diffuse ions backstreaming from the
855 Earth's bow shock 2. Origin. *Journal of Geophysical Research: Space Physics (1978–*
856 *2012)*, *86*(A6), 4405–4413.
- 857 Bonifazi, C., Moreno, G., Lazarus, A. J., & Sullivan, J. D. (1980, November). Deceleration
858 of the solar wind in the earth's foreshock region - ISEE 2 and IMP 8 observations.
859 *textbackslashjgr*, *85*, 6031–6038. doi: 10.1029/JA085iA11p06031
- 860 Brackbill, J. U. (2011). A comparison of fluid and kinetic models of steady magnetic
861 reconnection. *Physics of Plasmas (1994-present)*, *18*(3), 032309. doi: 10.1063/1
862 .3568828
- 863 Buneman, O., Neubert, T., & Nishikawa, K.-I. (1992). Solar wind-magnetosphere interaction
864 as simulated by a 3-d em particle code. *IEEE transactions on plasma science*, *20*(6),
865

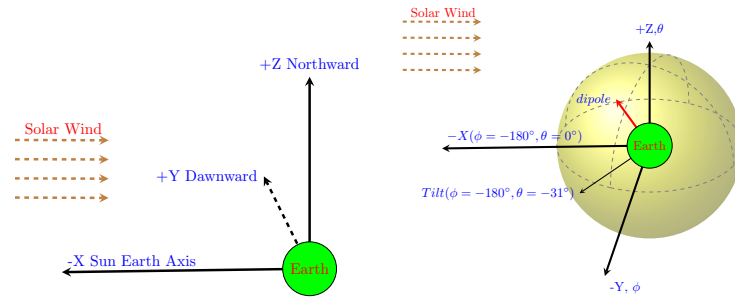
- 866 810–816.
- 867 Cai, D., Esmaili, A., Lembège, B., & Nishikawa, K.-I. (2015). Cusp dynamics under
868 northward imf using three-dimensional global particle-in-cell simulations. *Journal of*
869 *Geophysical Research: Space Physics*, *120*(10), 8368–8386.
- 870 Cai, D., Li, Y., Nishikawa, K.-I., Xiao, C., Yan, X., & Pu, Z. (2003). Parallel 3-D Elec-
871 tromagnetic Particle Code Using High Performance FORTRAN: Parallel TRISTAN.
872 In *Space Plasma Simulation* (Vol. 615, pp. 25–53). Springer Berlin Heidelberg. doi:
873 10.1007/3-540-36530-3.2
- 874 Chang, Q., Xu, X., Xu, Q., Zhong, J., Xu, J., Wang, J., & Zhang, T. (2019). Multiple-point
875 modeling the parker spiral configuration of the solar wind magnetic field at the solar
876 maximum of solar cycle 24. *The Astrophysical Journal*, *884*(2), 102.
- 877 Cohen, O., Ma, Y., Drake, J. J., Glocer, A., Garraffo, C., Bell, J. M., & Gombosi, T. I.
878 (2015, jun). THE INTERACTION OF VENUS-LIKE, m-DWARF PLANETS WITH
879 THE STELLAR WIND OF THEIR HOST STAR. *The Astrophysical Journal*, *806*(1),
880 41. Retrieved from [https://doi.org/10.1088/](https://doi.org/10.1088/0004-637x/806/1/41)
881 [0004-637x/806/1/41](https://doi.org/10.1088/0004-637x/806/1/41) doi: 10.1088/
882 0004-637x/806/1/41
- 883 Cohen, O., Moschou, S.-P., Glocer, A., Sokolov, I. V., Mazeh, T., Drake, J. J., ... Alvarado-
884 Gómez, J. D. (2018, oct). Exoplanet modulation of stellar coronal radio emission.
885 *The Astronomical Journal*, *156*(5), 202. Retrieved from [https://doi.org/10.3847/](https://doi.org/10.3847/1538-3881/aae1f2)
886 [1538-3881/aae1f2](https://doi.org/10.3847/1538-3881/aae1f2) doi: 10.3847/1538-3881/aae1f2
- 887 Dimmock, A., Nykyri, K., Osmane, A., Karimabadi, H., & Pulkkinen, T. (2017). Dawn-
888 dusk asymmetries of the earth's dayside magnetosheath in the magnetosheath inter-
889 planetary medium reference frame. *Dawn-Dusk Asymmetries in Planetary Plasma*
890 *Environments*, 49–72.
- 891 Dimmock, A. P., Nykyri, K., Karimabadi, H., Osmane, A., & Pulkkinen, T. I. (2015, April).
892 A statistical study into the spatial distribution and dawn-dusk asymmetry of dayside
893 magnetosheath ion temperatures as a function of upstream solar wind conditions.
894 *Journal of Geophysical Research (Space Physics)*, *120*(4), 2767–2782. doi: 10.1002/
895 2014JA020734
- 896 Dimmock, A. P., Nykyri, K., & Pulkkinen, T. I. (2014, August). A statistical study of
897 magnetic field fluctuations in the dayside magnetosheath and their dependence on
898 upstream solar wind conditions. *Journal of Geophysical Research (Space Physics)*,
899 *119*(8), 6231–6248. doi: 10.1002/2014JA020009
- 900 Dušík, Š., Granko, G., Šafránková, J., Němeček, Z., & Jelínek, K. (2010). Imf cone angle
901 control of the magnetopause location: Statistical study. *Geophysical Research Letters*,
902 *37*(19).
- 903 Eastwood, J. P. (2008). The science of space weather. *Philosophical Transactions of the*
904 *Royal Society A: Mathematical, Physical and Engineering Sciences*, *366*(1884), 4489–
905 4500.
- 906 Fairfield, D., Baumjohann, W., Paschmann, G., Lühr, H., & Sibeck, D. (1990). Upstream
907 pressure variations associated with the bow shock and their effects on the magneto-
908 sphere. *Journal of Geophysical Research: Space Physics*, *95*(A4), 3773–3786.
- 909 Garcia, K., & Hughes, W. (2007). Finding the lyon-fedder-mobarry magnetopause: A
910 statistical perspective. *Journal of Geophysical Research: Space Physics*, *112*(A6).
- 911 Gingell, P. W., Burgess, D., & Matteini, L. (2015, March). The Three-dimensional Evolution
912 of Ion-scale Current Sheets: Tearing and Drift-kink Instabilities in the Presence of
913 Proton Temperature Anisotropy. *The Astrophysical Journal*, *802*(1), 4. doi: 10.1088/
914 0004-637X/802/1/4
- 915 Greenstadt, E. W., Green, I. M., Inouye, G. T., Hundhausen, A. J., Bame, S. J., & Strong,
916 I. B. (1968, January). Correlated magnetic field and plasma observations of the Earth's
917 bow shock. *Journal of Geophysical Research*, *73*, 51. doi: 10.1029/JA073i001p00051
- 918 Grygorov, K., Šafránková, J., Němeček, Z., Pi, G., Přech, L., & Urbář, J. (2017). Shape
919 of the equatorial magnetopause affected by the radial interplanetary magnetic field.
920 *Planetary and Space Science*, *148*, 28–34.
- 921 Haaland, S., Lybekk, B., Maes, L., Laundal, K., Pedersen, A., Tenfjord, P., ... Snekvik,

- 921 K. (2017). North-south asymmetries in cold plasma density in the magnetotail lobes:
 922 Cluster observations. *Journal of Geophysical Research: Space Physics*, *122*(1), 136–
 923 149.
- 924 Haaland, S., Reistad, J., Tenfjord, P., Gjerloev, J., Maes, L., DeKeyser, J., ... Dorville, N.
 925 (2014). Characteristics of the flank magnetopause: Cluster observations. *Journal of*
 926 *Geophysical Research: Space Physics*, *119*(11), 9019–9037.
- 927 Haaland, S., Runov, A., Artemyev, A., & Angelopoulos, V. (2019). Characteristics of the
 928 flank magnetopause: Themis observations. *Journal of Geophysical Research: Space*
 929 *Physics*, *124*(5), 3421–3435.
- 930 Heikkila, W. J. (2011). *Earth's Magnetosphere: Formed by the Low-latitude Boundary*
 931 *Layer*. Elsevier.
- 932 Jacobsen, K. S., Phan, T. D., Eastwood, J. P., Sibeck, D. G., Moen, J. I., Angelopoulos, V.,
 933 ... Fornaçon, K.-H. (2009). THEMIS observations of extreme magnetopause motion
 934 caused by a hot flow anomaly. *Journal of Geophysical Research (Space Physics)*, *114*,
 935 8210. Retrieved from <http://adsabs.harvard.edu/abs/2009JGRA...114.8210J>
- 936 Jelínek, K., Němeček, Z., Šafránková, J., Shue, J.-H., Suvorova, A. V., & Sibeck, D. G.
 937 (2010). Thin magnetosheath as a consequence of the magnetopause deformation:
 938 THEMIS observations. *Journal of Geophysical Research (Space Physics)*, *115*, 10203.
 939 Retrieved from <http://adsabs.harvard.edu/abs/2010JGRA...11510203J>
- 940 Johnson, J. R., Wing, S., & Delamere, P. A. (2014). Kelvin helmholtz instability in planetary
 941 magnetospheres. *Space Science Reviews*, *184*(1-4), 1–31.
- 942 Karimabadi, H., Krauss-Varban, D., Huba, J., & Vu, H. (2004). On magnetic reconnection
 943 regimes and associated three-dimensional asymmetries: Hybrid, hall-less hybrid, and
 944 hall-mhd simulations. *Journal of Geophysical Research: Space Physics*, *109*(A9).
- 945 Karimabadi, H., Roytershteyn, V., Vu, H. X., Omelchenko, Y. A., Scudder, J., Daughton,
 946 W., ... Geveci, B. (2014). The link between shocks, turbulence, and magnetic re-
 947 connection in collisionless plasmas. *Physics of Plasmas*, *21*, 062308. doi: 10.1063/
 948 1.4882875
- 949 Lavraud, B., Borovsky, J. E., Génot, V., Schwartz, S. J., Birn, J., Fazakerley, A. N., ...
 950 Wild, J. A. (2009). Tracing solar wind plasma entry into the magnetosphere using
 951 ion-to-electron temperature ratio. *Geophys. Res. Lett.*, *36*, 18109. Retrieved from
 952 <http://adsabs.harvard.edu/abs/2009GeoRL...3618109L>
- 953 Le Contel, O., Retinò, A., Breuillard, H., Mirioni, L., Robert, P., Chasapis, A., ... Saito,
 954 Y. (2016, June). Whistler mode waves and Hall fields detected by MMS during
 955 a dayside magnetopause crossing. *Geophysical Research Letters*, *43*(12), 5943-5952.
 956 doi: 10.1002/2016GL068968
- 957 Lindman, E. (1975). “Free-space” boundary conditions for the time dependent wave equa-
 958 tion. *J. Comput. Phys.*, *18*(1), 66–78.
- 959 Liu, Y.-H., Li, T., Hesse, M., Sun, W., Liu, J., Burch, J., ... Huang, K. (2019). Three-
 960 dimensional magnetic reconnection with a spatially confined x-line extent: Implica-
 961 tions for dipolarizing flux bundles and the dawn-dusk asymmetry. *Journal of Geo-*
 962 *physical Research: Space Physics*, *124*(4), 2819–2830.
- 963 Lu, J., Wang, M., Kabin, K., Zhao, J., Liu, Z.-Q., Zhao, M., & Li, G. (2015). Pressure
 964 balance across the magnetopause: Global mhd results. *Planetary and Space Science*,
 965 *106*, 108–115.
- 966 Lu, S., Lin, Y., Angelopoulos, V., Artemyev, A., Pritchett, P., Lu, Q., & Wang, X. (2016).
 967 Hall effect control of magnetotail dawn-dusk asymmetry: A three-dimensional global
 968 hybrid simulation. *Journal of Geophysical Research: Space Physics*, *121*(12), 11–882.
- 969 Luo, H., Chen, G., Du, A., & Xu, W. (2013). Solar wind dependence of energy coupling
 970 between solar wind and magnetosphere during intense northward imfs. *Planetary and*
 971 *Space Science*, *79*, 82–89.
- 972 Masters, A., Slavin, J., DiBraccio, G., Sundberg, T., Winslow, R., Johnson, C., ... Korth,
 973 H. (2013). A comparison of magnetic overshoots at the bow shocks of mercury and
 974 saturn. *Journal of Geophysical Research: Space Physics*, *118*(7), 4381–4390.
- 975 Merka, J., Szabo, A., Šafránková, J., & Němeček, Z. (2003). Earth's bow shock and

- 976 magnetopause in the case of a field-aligned upstream flow: Observation and model
 977 comparison. *Journal of Geophysical Research: Space Physics (1978–2012)*, 108(A7),
 978 –.
- 979 Němeček, Z., Šafránková, J., Zastenker, G. N., Pišoft, P., & Jelínek, K. (2002, April).
 980 Low-frequency variations of the ion flux in the magnetosheath. *Planetary and Space*
 981 *Science*, 50(5-6), 567-575. doi: 10.1016/S0032-0633(02)00036-3
- 982 Omid, N., Blanco-Cano, X., Russell, C. T., & Karimabadi, H. (2004, January). Dipolar
 983 magnetospheres and their characterization as a function of magnetic moment. *Ad-*
 984 *vances in Space Research*, 33, 1996–2003. doi: 10.1016/j.asr.2003.08.041
- 985 Østgaard, N., Mende, S., Frey, H., Frank, L., & Sigwarth, J. (2003). Observations of
 986 non-conjugate theta aurora. *Geophysical Research Letters*, 30(21).
- 987 Palmroth, M., Ganse, U., Pfau-Kempf, Y., Battarbee, M., Turc, L., Brito, T., ... von
 988 Althaus, S. (2018, August). Vlasov methods in space physics and astrophysics. *Living*
 989 *Reviews in Computational Astrophysics*, 4(1), 1. doi: 10.1007/s41115-018-0003-2
- 990 Paral, J., & Rankin, R. (2013). Dawn–dusk asymmetry in the kelvin–helmholtz instability
 991 at mercury. *Nature Communications*, 4(1), 1–5.
- 992 Park, J.-S., Shue, J.-H., Kim, K.-H., Pi, G., Němeček, Z., & Šafránková, J. (2016, July).
 993 Global expansion of the dayside magnetopause for long-duration radial IMF events:
 994 Statistical study on GOES observations. *Journal of Geophysical Research (Space*
 995 *Physics)*, 121(7), 6480–6492. doi: 10.1002/2016JA022772
- 996 Parks, G. K. (1991). Physics of space plasmas—an introduction. *Redwood City, CA, Addison-*
 997 *Wesley Publishing Co., 1991, 547 p.*
- 998 Paschmann, G., Scopke, N., Papamastorakis, I., Asbridge, J., Bame, S., & Gosling, J.
 999 (1981). Characteristics of reflected and diffuse ions upstream from the earth’s bow
 1000 shock. *Journal of Geophysical Research: Space Physics (1978–2012)*, 86(A6), 4355–
 1001 4364.
- 1002 Paularena, K., Richardson, J., Kolpak, M., Jackson, C., & Siscoe, G. (2001). A dawn-dusk
 1003 density asymmetry in earth’s magnetosheath. *Journal of Geophysical Research: Space*
 1004 *Physics*, 106(A11), 25377–25394.
- 1005 Pi, G., Němeček, Z., Šafránková, J., Grygorov, K., & Shue, J.-H. (2018). Formation of
 1006 the dayside magnetopause and its boundary layers under the radial IMF. *Journal of*
 1007 *Geophysical Research: Space Physics*, 123(5), 3533–3547.
- 1008 Samsonov, A. (2006, January). Numerical modelling of the Earth’s magnetosheath for
 1009 different IMF orientations. *Advances in Space Research*, 38(8), 1652-1656. doi: 10
 1010 .1016/j.asr.2005.06.009
- 1011 Samsonov, A. A. (2011, January). Propagation of inclined interplanetary shock through
 1012 the magnetosheath. *Journal of Atmospheric and Solar-Terrestrial Physics*, 73, 30–39.
 1013 doi: 10.1016/j.jastp.2009.10.014
- 1014 Samsonov, A. A., Bogdanova, Y. V., Branduardi-Raymont, G., Sibeck, D. G., & Toth, G.
 1015 (2020). Is the Relation Between the Solar Wind Dynamic Pressure and the Mag-
 1016 netopause Standoff Distance so Straightforward? *Geophys. Res. Lett.*, 47(8). doi:
 1017 10.1029/2019GL086474
- 1018 Samsonov, A. A., Němeček, Z., Šafránková, J., & Jelínek, K. (2012, May). Why does the
 1019 subsolar magnetopause move sunward for radial interplanetary magnetic field? *Jour-*
 1020 *nal of Geophysical Research (Space Physics)*, 117, 5221. doi: 10.1029/2011JA017429
- 1021 Samsonov, A. A., Sibeck, D. G., Šafránková, J., Němeček, Z., & Shue, J. H. (2017,
 1022 March). A method to predict magnetopause expansion in radial IMF events by MHD
 1023 simulations. *Journal of Geophysical Research (Space Physics)*, 122(3), 3110-3126. doi:
 1024 10.1002/2016JA023301
- 1025 Shue, J. H., Chao, J. K., Fu, H. C., Russell, C. T., Song, P., Khurana, K. K., & Singer,
 1026 H. J. (1997, May). A new functional form to study the solar wind control of the mag-
 1027 netopause size and shape. *Journal of Geophysical Research (Space Physics)*, 102(A5),
 1028 9497-9512. doi: 10.1029/97JA00196
- 1029 Shue, J.-H., Chao, J.-K., Song, P., McFadden, J., Suvorova, A., Angelopoulos, V., ...
 1030 Plaschke, F. (2009). Anomalous magnetosheath flows and distorted subsolar mag-

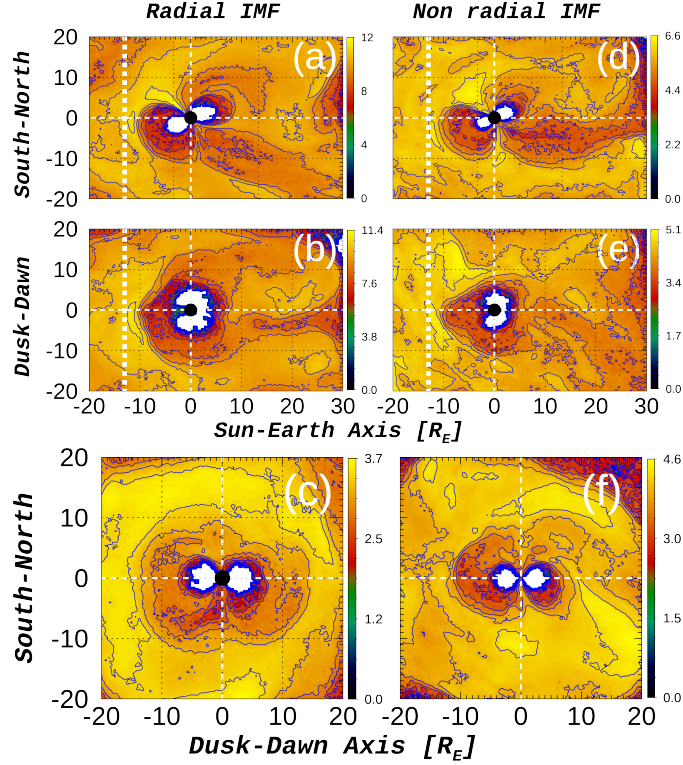
- 1031 netopause for radial interplanetary magnetic fields. *Geophysical Research Letters*,
 1032 *36*(18).
- 1033 Sibeck, D. G., Allen, R., Aryan, H., Bodewits, D., Brandt, P., Branduardi-Raymont, G.,
 1034 ... others (2018). Imaging plasma density structures in the soft x-rays generated by
 1035 solar wind charge exchange with neutrals. *Space Science Reviews*, *214*(4), 79.
- 1036 Sibeck, D. G., Decker, R. B., Mitchell, D. G., Lazarus, A. J., Lepping, R. P., & Szabo,
 1037 A. (2001). Solar wind preconditioning in the flank foreshock: IMP 8 observations.
 1038 *J. Geophys. Res.*, *106*, 21675–21688. Retrieved from [http://adsabs.harvard.edu/
 1039 abs/2001JGR...10621675S](http://adsabs.harvard.edu/abs/2001JGR...10621675S)
- 1040 Sorathia, K., Merkin, V., Ukhorskiy, A., Allen, R., Nykyri, K., & Wing, S. (2019). Solar
 1041 wind ion entry into the magnetosphere during northward imf. *Journal of Geophysical
 1042 Research: Space Physics*, *124*(7), 5461–5481.
- 1043 Spreiter, J. R., & Alksne, A. Y. (1969). Plasma flow around the magnetosphere. *Reviews
 1044 of Geophysics*, *7*(1-2), 11–50.
- 1045 Suvorova, A., & Dmitriev, A. (2015). Magnetopause inflation under radial imf: Comparison
 1046 of models. *Earth and Space Science*, *2*(4), 107–114.
- 1047 Suvorova, A. V., Shue, J. H., Dmitriev, A. V., Sibeck, D. G., McFadden, J. P., Hasegawa,
 1048 H., ... Němeček, Z. (2010, October). Magnetopause expansions for quasi-radial inter-
 1049 planetary magnetic field: THEMIS and Geotail observations. *Journal of Geophysical
 1050 Research (Space Physics)*, *115*(A10), A10216. doi: 10.1029/2010JA015404
- 1051 Tan, B., Lin, Y., Perez, J., & Wang, X. (2011). Global-scale hybrid simulation of dayside
 1052 magnetic reconnection under southward imf: Structure and evolution of reconnection.
 1053 *Journal of Geophysical Research: Space Physics*, *116*(A2).
- 1054 Trattner, K., Mulcock, J., Petrinec, S., & Fuselier, S. (2007). Location of the reconnection
 1055 line at the magnetopause during southward imf conditions. *Geophysical Research
 1056 Letters*, *34*(3).
- 1057 Treumann, R. A., & Baumjohann, W. (2013). Collisionless magnetic reconnection in space
 1058 plasmas. *Frontiers in Physics*, *1*, 31.
- 1059 Tsurutani, B. T., & Lakhina, G. S. (1997). Some basic concepts of wave-particle interactions
 1060 in collisionless plasmas. *Reviews of Geophysics*, *35*(4), 491–501.
- 1061 Turc, L., Tarvus, V., Dimmock, A., Battarbee, M., Ganse, U., Johlander, A., ... Palm-
 1062 roth, M. (2020). Asymmetries in the earth's dayside magnetosheath: results
 1063 from global hybrid-vlasov simulations. *Annales Geophysicae Discussions*, *2020*, 1–
 1064 24. Retrieved from <https://www.ann-geophys-discuss.net/angeo-2020-13/> doi:
 1065 10.5194/angeo-2020-13
- 1066 Turner, D., Wilson, L., Liu, T., Cohen, I., Schwartz, S., Osmane, A., ... others (2018).
 1067 Autogenous and efficient acceleration of energetic ions upstream of earth's bow shock.
 1068 *Nature*, *561*(7722), 206–210.
- 1069 Villasenor, J., & Buneman, O. (1992). Rigorous charge conservation for local electromag-
 1070 netic field solvers. *Comput. Phys. Commun.*, *69*(2), 306–316.
- 1071 Šafránková, J., Němeček, Z., Santolík, O., Sibeck, D. G., Zastenker, G. N., & Skalsky,
 1072 A. (2000). The Flank Magnetopause: Interball Observations. *Advances in Space Re-
 1073 search*, *25*, 1503–1510. Retrieved from [http://adsabs.harvard.edu/abs/2000AdSpR
 1074 ..25.1503S](http://adsabs.harvard.edu/abs/2000AdSpR...25.1503S)
- 1075 Walsh, A. P., Haaland, S., Forsyth, C., Keese, A. M., Kissinger, J., Li, K., ... Taylor,
 1076 M. G. G. T. (2014, July). Dawn-dusk asymmetries in the coupled solar wind-
 1077 magnetosphere-ionosphere system: a review. *Annales Geophysicae*, *32*, 705–737.
 1078 Retrieved from <https://ui.adsabs.harvard.edu/abs/2014AnGeo...32..705W> doi:
 1079 10.5194/angeo-32-705-2014
- 1080 Walsh, B. M. (2017). Magnetopause plasma parameters and asymmetries in solar wind-
 1081 magnetosphere coupling. *Dawn-Dusk Asymmetries in Planetary Plasma Environ-
 1082 ments*, 29–39.
- 1083 Walsh, B. M., Sibeck, D. G., Wang, Y., & Fairfield, D. H. (2012, December). Dawn-dusk
 1084 asymmetries in the Earth's magnetosheath. *Journal of Geophysical Research (Space
 1085 Physics)*, *117*(A12), A12211. doi: 10.1029/2012JA018240

- 1086 Wang, C.-P., Lyons, L. R., Weygand, J. M., Nagai, T., & McEntire, R. W. (2006). Equatorial
1087 distributions of the plasma sheet ions, their electric and magnetic drifts, and
1088 magnetic fields under different interplanetary magnetic field b_z conditions. *Journal of*
1089 *Geophysical Research: Space Physics*, *111*(A4).
- 1090 Wang, J., Guo, Z., Ge, Y. S., Du, A., Huang, C., & Qin, P. (2018, October). The responses
1091 of the earth's magnetopause and bow shock to the IMF B_z and the solar wind dynamic
1092 pressure: a parametric study using the AMR-CESE-MHD model. *Journal of Space*
1093 *Weather and Space Climate*, *8*, A41. doi: 10.1051/swsc/2018030
- 1094 Wang, Y.-M., Grappin, R., Robbrecht, E., & Sheeley Jr, N. (2012).
1095 *The Astrophysical Journal*, *749*(2), 182.
- 1096 Willis, D. (1978). The magnetopause: Microstructure and interaction with magnetospheric
1097 plasma. *Journal of Atmospheric and Terrestrial Physics*, *40*(3), 301–322.
- 1098 Wing, S., Johnson, J. R., Chaston, C. C., Echim, M., Escoubet, C. P., Lavraud, B., ...
1099 Wang, C. P. (2014, November). Review of Solar Wind Entry into and Transport
1100 Within the Plasma Sheet. *Space Science Reviews*, *184*(1-4), 33-86. doi: 10.1007/
1101 s11214-014-0108-9
- 1102 Yu, Y., & Ridley, A. J. (2009, December). The response of the magnetosphere-ionosphere
1103 system to a sudden dynamic pressure enhancement under southward IMF conditions.
1104 *Annales Geophysicae*, *27*(12), 4391-4407. doi: 10.5194/angeo-27-4391-2009
- 1105 Zhang, H., Fu, S., Pu, Z., Lu, J., Zhong, J., Zhu, C., ... Liu, L. (2019, aug). Statistics
1106 on the magnetosheath properties related to magnetopause magnetic reconnection.
1107 *The Astrophysical Journal*, *880*(2), 122. Retrieved from [https://doi.org/](https://doi.org/10.3847/1538-4357/ab290e)
1108 [10.3847/1538-4357/ab290e](https://doi.org/10.3847/1538-4357/ab290e) doi: 10.3847/1538-4357/ab290e



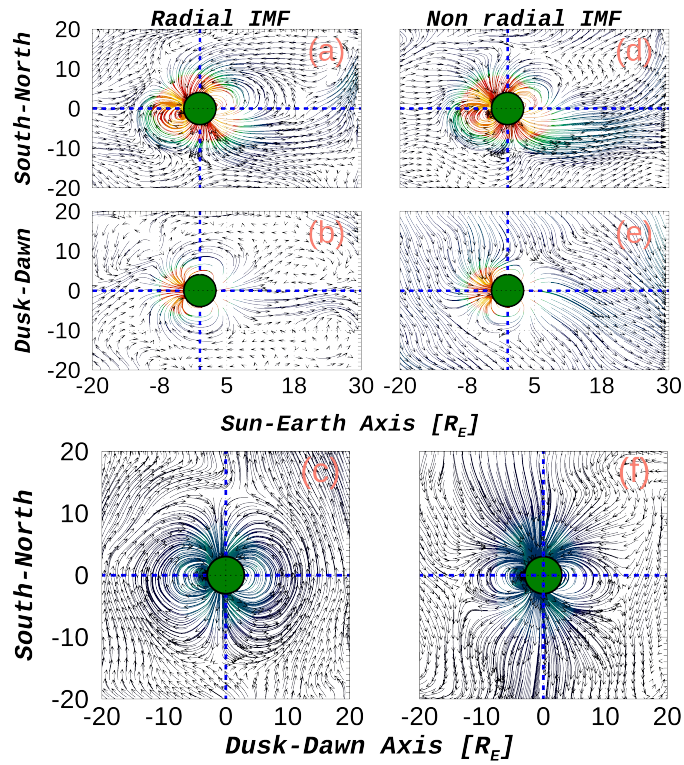
1

Figure 1. Code coordinates scheme (left) and spherical coordinates illustration used in MP derivation (right)



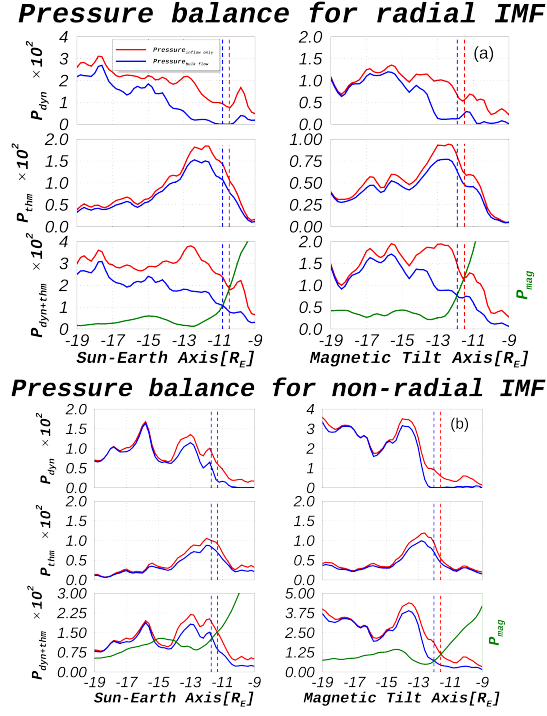
1

Figure 2. Solar wind 2D density contours in the XZ ($Y=0$), XY ($Z=0$), and YZ ($X=0$) planes for both IMF orientations. Vertical dashed lines at $X = -13R_E$ indicate the position of linear density profiles shown in Fig. 8. Panels (a), (b), and (c) are for radial IMF and panels (d), (e), and (f) are for non-radial IMF



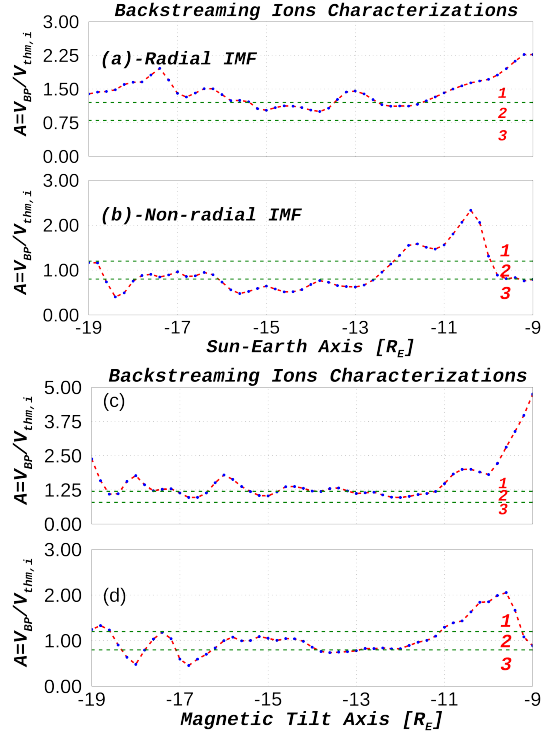
1

Figure 3. Fields 2D topology in the XZ ($Y=0$), XY ($Z=0$), and YZ ($X=0$) planes for both IMF orientations. Panels (a), (b), and (c) are for radial IMF and panels (d), (e), and (f) are for non radial IMF



1

Figure 4. MP size derivation from pressure balance system measured radially at two locations. The MP is derived along the Earth-Sun axis (OX) and along the tilted magnetic equatorial axis. Bulk flow (blue) and inflow (red) pressures show different MP locations. For radial IMF, panel (a), it is found that $MP = [-10.8, -10.5] R_E$ derived with bulk and inflow pressures only along Sun-Earth Axis and $MP = [-11.9, -11.5] R_E$ along the tilted magnetic equatorial axis. Respectively for non-radial IMF, panel (b), $MP = [-11.7, -11.3]$ and $[-12., -11.6] R_E$.



1

Figure 5. Characterization of backstreaming ions in the dayside magnetosphere based on their bulk flow ratio on thermal speed (Adopted from (Bonifazi & Moreno, 1981b)). Panels, a and b are taken along OX-axis in XZ plane and panels c, and d are taken along tilted magnetic equatorial axis for both IMF orientations. This figure shows the reflected and diffuse fractions of the backstreaming ions (their respective percentages are shown in table 5). Scaling factor "A" is used for the characterization of backstreaming ions. $A > 1.2$ denotes reflected ions(region-1) in the plots. $A < 0.8$ denotes diffuse ions(region-3). $0.8 < A < 1.2$ denotes intermediate ions(region-2)

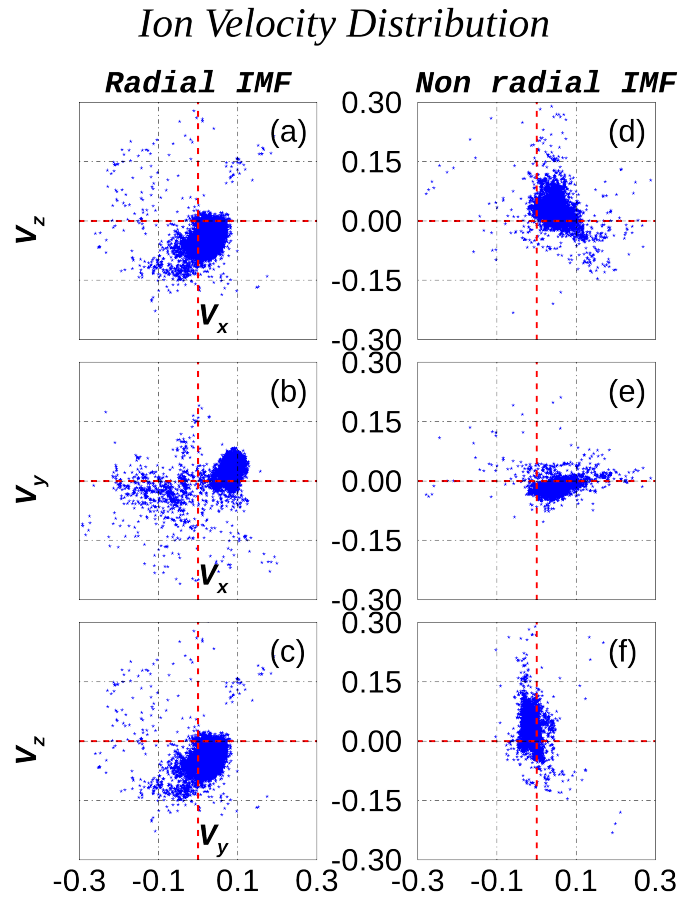
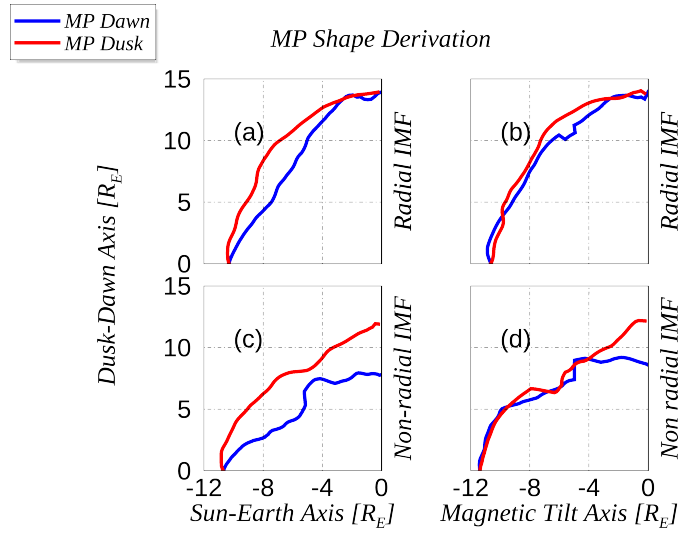
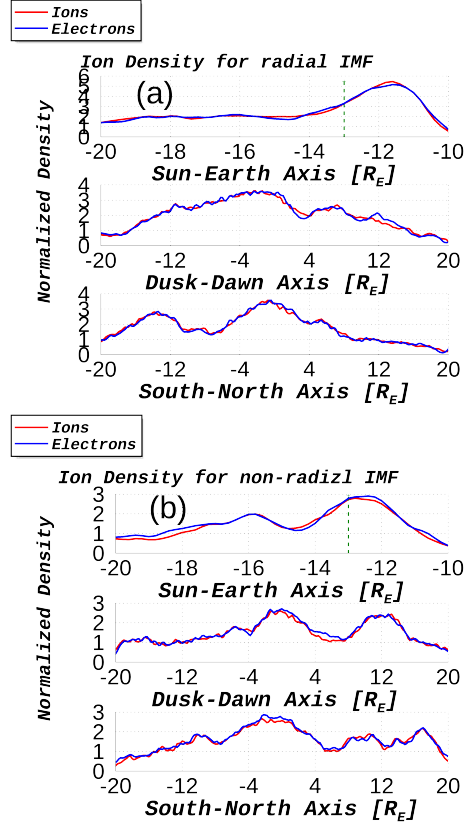


Figure 6. Ion Velocity dayside distribution measured from $-20R_E$ to the planet position ($z=y=0$) along Sun-Earth axis. Left panels are for radial IMF and right panels are for non radial IMF orientation.



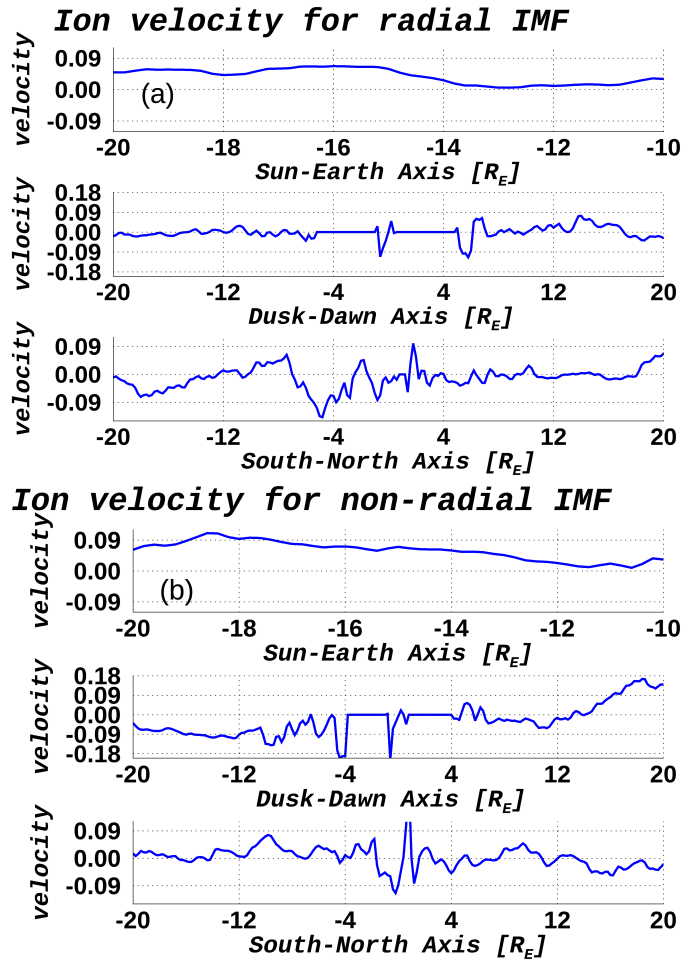
1

Figure 7. Panels (a) and (b) show the MP shape for radial IMF along Sun-Earth and tilted magnetic equatorial axis. Similarly, panels (c) and (d) are the same but for non-radial IMF. We remark that the size shown here is approximately equivalent to the MP sizes derived from the density steepening.



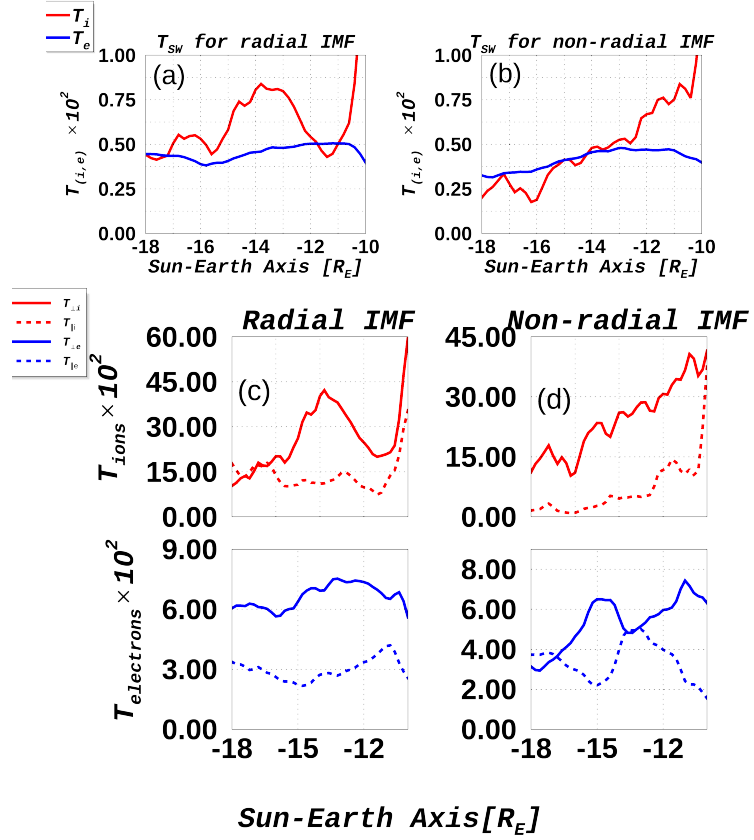
1

Figure 8. Ion and electron densities are plotted in three directions, along OX ($Y=Z=0$), OY ($X=-13$, and $Z=0$), and OZ ($X=-13$, and $Y=0$), just outside the MP for radial IMF in panel a and for non-radial IMF in panel b. Their values are normalized to the initial densities. The density profile is plotted only in the dayside region as shown with vertical dashed lines (at $X = -13R_E$) in Fig. 2. This figure also shows the plasma quasi neutrality.



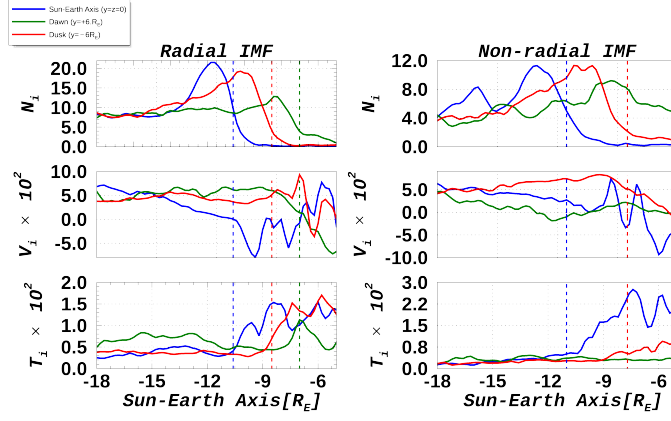
1

Figure 9. Bulk ion velocity modulus for both IMF orientations are plotted along three directions as in Fig. 8.



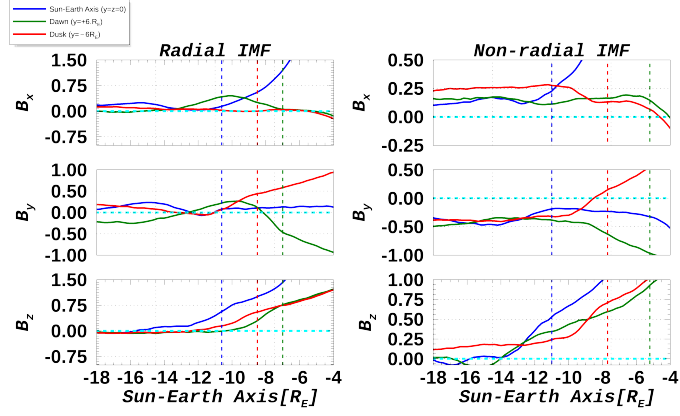
1

Figure 10. Ion and electron temperatures are shown in the dayside magnetosphere for both IMF orientations (panels a and b). The average ion to electron temperature ratios in the magnetosheath between -14 and $-12.5R_E$ are $\langle T_i/T_e \rangle = 1.72$ and $\langle T_i/T_e \rangle = 1.1$ for radial (panel a) and non-radial IMF (panel b), respectively. Temperature anisotropy for ions and electrons for both IMF orientations are shown in panel c and d. The $T_{\perp i}/T_{\parallel i}$, and $T_{\perp e}/T_{\parallel e}$ ratios averaged between -18 to $-10R_E$ are (2,2.3) respectively for radial IMF. This ratio reads (6,1.8) for non-radial IMF.



1

Figure 11. Ion density, velocity, and temperature (N_i , V_i , T_i) are plotted along the OX-axis and at ± 6 on both dusk and dawn directions in the XY plane. Vertical dashed lines show the MP position at the subsolar point (blue), dusk flank (red), and dawn flank (green) quantities show dusk-dawn asymmetry at the $\pm 6R_E$.



1

Figure 12. IMF components, B_x , B_y , and B_z are plotted along the OX-axis and at ± 6 on both dawn and dusk directions in the XY plane. Vertical dashed lines show the MP position at the subsolar point (blue), dusk flank (red), and dawn flank (green) quantities show dusk-dawn asymmetry at the $\pm 6R_E$. Horizontal cyan dashed line shows the zero value of IMF. Change of IMF polarity is significantly seen in B_y component.